THEORY AND CALCULATION FOR DISPLACEMENTS AND STRESSES AT AN EARTHQUAKE SOURCE

Paul G. Richards

Lamont-Doherty Geological Observatory

Prepared for:

Air Force Office of Scientific Research
Advanced Research Projects Agency

30 October 1974

UNCLASSIFIED

SECURITY CLASSIFICATION OF THIS PAGE (When Data Entered)

REPORT DOCUMENTATION PAGE		READ INSTRUCTIONS BEFORE COMPLETING FORM
1. REPORT NUMBER AFOSR - TR - 75 - 0202	2. GOVT ACCESSION NO.	3. RECIPIENT'S CATALOG NUMBER AD/A-004827
4. TITLE (and Subtitle) THEORY AND CALCULATION FOR DISPLACEMENTS AND STRESSES AT AN EARTHQUAKE SOURCE		5. TYPE OF REPORT & PERIOD COVERED Semi-Annual, Scientific, interim 6. PERFORMING ORG. REPORT NUMBER
7. AUTHOR(s) Professor Paul G. Richards		8. CONTRACT OR GRANT NUMBER(s) F44620-74-C-0029
9. PERFORMING ORGANIZATION NAME AND ADDRESS Columbia University Lamont-Doherty Geological Observatory Palisades, New York 10964		10. PROGRAM ELEMENT, PROJECT, TASK AREA & WORK UNIT NUMBERS ARPA Order No. 1827-11 Program Code No. 4F10 Program Element Code 62701
11. CONTROLLING OFFICE NAME AND ADDRESS Advanced Research Projects Agency 1400 Wilson Boulevard Arlington, Virginia 22209		12. REPORT DATE 30 October 1974 13. NUMBER OF PAGES 79
14. MONITORING AGENCY NAME & ADDRESS (if different from Controlling Office) Air Force Office of Scientific Research/NP 1400 Wilson Boulevard Arlington, Virginia 22209		15. SECURITY CLASS. (of this report) UNCLASSIFIED 15a. DECLASSIFICATION/DOWNGRADING SCHEDULE

16. DISTRIBUTION STATEMENT (of this Report)

Approved for public release: distribution unlimited

17. DISTRIBUTION STATEMENT (of the abstract entered in Block 20, if different from Report)

18. SUPPLEMENTARY NOTES

19. KEY WORDS (Continue on reverse side if necessary and identify by block number)

Earthquake - explosion discrimination

Earthquake source theory

20. ABSTRACT (Continue on reverse side if necessary and identify by block number)

This progress report describes the near-field motions of an earthquake source model which is governed by simple physical constraints in terms of dynamic friction on a fault plane. It also describes a computer program which will calculate the displacements radiated (into the near, intermediate, and far field) by any of a wide variety of earthquake fault motions. Several applications of the program are described.

DD FORM 1 JAN 73 1473 EDITION OF 1 NOV 65 IS OBSOLETE

UNCLASSIFIED

ARPA Order Number:	1827-11
Program Code Number:	4F10
Contractor:	Columbia University
Effective Date of Contract:	1 October 1973
Contract Expiration Date:	30 September 1975
Amount of Contract:	$70,000.00
Contract Number:	F 44620-74-C-0029
Principal Investigator:	Paul G. Richards, 914-359-2900
Program Manager:	Paul G. Richards, 914-359-2900
Title of Work:	Displacements and Stresses for an Earthquake Source

SUMMARY

During the second six months of the subject contract, the purpose of the research program was to investigate properties of an earthquake source, to provide a physical basis for discrimination between different types of seismic events. The two main approaches used were:

1. To investigate thoroughly the only known analytic solution for a three dimensional problem of earthquake faulting, in which shear stresses on the moving parts of the fault surface are determined by a simple law of friction.

2. To develop the computational capability to determine the seismograms which would result from any assumption about the relative shearing motions taking place across an earthquake fault.

Research on the first of these approaches is based on modeling the rupture process of earthquake faulting by a shear crack. The shear stress, on moving faces of the crack, is taken as a constant (the dynamic coefficient of friction) times the normal stress acting across the crack. The crack is presumed to grow from a point (i.e., the point at which rupture begins on an earthquake fault), and then grows steadily as an ellipse with fixed eccentricity. The great virtue of this earthquake model is that it is based on very simple physical principles of mechanical failure, and no a priori assumption is made about the displacement on the crack surface itself. The resulting accelerations can be found everywhere within the elastic medium. Principal properties of the computed

solution are: (i) that particle velocities, near the rupture front, increase with increasing distance from the point of initial rupture; (ii) that it is exceedingly difficult to detect any features in a record section of near-field seismograms which will enable one to determine the rupture velocity; (iii) that the concept of "maximum acceleration", observed in the near field for a given earthquake, is an unstable property of the positioning of the observing point within the radiation pattern, rather than a macroscopic property of the earthquake itself.

The goal of our second major research approach has been fully attained. That is, we have developed a computer program to find the seismograms which would result from virtually any earthquake source, described in terms of the rupture velocities and relative displacements taking place on a fault plane within an infinite homogeneous elastic medium. We have used this program extensively to examine the ground motion which would take place near an earthquake fault for several dislocation models of the earthquake. Quite different dislocation models can give very similar displacements at stations located only one fault dimension from the fault. In particular: 1) models with fault motions and rupture geometry quite different from Haskell's propagating ramp can often have near-field motions very similar to those from a ramp model; and 2) quite similar near-field motions are found, for different ramp models in which the rupture velocity and rise time are varied together over rather large ranges (e.g., a factor of three in rise time).

We infer that there is considerable ambiguity in interpreting near-field displacement data in terms of a model of fault motion. The ambiguity may be reduced by using acceleration data, although this entails a considerable increase in computer time for solving forward problems.

Both of our research approaches indicate a result which will be of importance in determining, from seismic data taken in the very near-field of a propagating fault, details of the fault motion itself. We have found that the component of (vector) displacement which is most sensitive to the fault motion is the component perpendicular to the fault surface. One might have expected that the most sensitive component would be that parallel to the direction of slip of the fault. Many experiments, particularly rock mechanics experiments, have emphasized measurement of fault motion parallel to the slip direction, but we find this is a component which is very insensitive to rupture velocity.

The two research approaches described above are each expected to lead to a research publication. Our efforts in the third six-month period of the contract will be directed towards problems in which the free surface of the earth has an important effect on waves radiating from an earthquake source.

Elastic Waves near the Rupture Front of a Growing Plane Elliptical Shear Crack:

A Three-Dimensional Solution

Earthquakes are a stress relaxation phenomenon: upon this, there has been general agreement among seismologists for over fifty

years. In this section, we describe a kind of fault motion which falls into this category, in which an initially high stress field is relieved by motion on the fault surface. We then describe the accelerations and displacements in the near-field of such a propagating fault.

We suppose that an infinite elastic medium is subjected to tectonic shearing stresses in the xz direction, with a fault in the plane z = 0. In this situation, a crack nucleates at a point, and a rupture front spreads steadily, initiating relative motion across the fault plane. We suppose that the rupture front maintains the shape of an ellipse, shown in Figure 1a, spreading steadily with speed σ in the x direction and speed ν in the y direction. This much of the description of earthquake faulting is "kinematic". However, the boundary condition we impose on fault plane is "dynamic". We suppose that dynamic friction forces act on those parts of the fault which are in relative motion: shearing stresses are taken to be proportional to the normal stress. It is often convenient to use spherical polar coordinates, shown in Figure 1b, rather than cartesian coordinates. Our computations are principally for points near the fault plane, since we are interested in trying to detect the presence of the rupture front as it moves past observing stations. Many of our computations are carried out for the case $\theta = 85°$. The rupture speed is taken as less even than the shear wave speed, so the only wave fronts in this problem are the spherical P and S wave fronts emanating from the point of initial nucleation. The rupture front itself does not radiate a wave

front.

These assumptions turn out to be enough to set up a boundary value problem for motions throughout the elastic medium. The solution has been published by Richards (1973), and here we are concerned with evaluating the solution to obtain insight into the behavior of shear stresses and accelerations in the vicinity of a propagating fault.

Figure 2 shows one of the quantities which can easily be computed. On the bottom left is shown a quadrant of the elliptical part of the fault, which is in motion. In this case, rupture in the x direction is taken as the Rayleigh speed, and in the y direction as the shear wave speed. The xz component of stress is being relieved by the fault, and the major part of the figure shows four different time histories for the stress rate $\dot{\tau}_{xz}$, at different azimuthal angles ϕ, for points near the fault plane. It is the stress rate which comes naturally out of the solution method, and it is natural to express the solution in a dimensionless form. The factors relating dimensionless and dimensioned stress rates and times are shown at the upper right of Figure 2: α, β and ρ are respectively the P wave speed, the shear wave speed, and the density; a is the particle velocity at the point of nucleation. Particular values of these dimensioning factors are shown, for a point 10 km away from the initial rupture, with an assumed particle velocity of 10 cm per second the initial rupture.

Figure 3 shows the result of time integrating Figure 2, to obtain τ_{xz} itself. Again, the shear stress is plotted in dimensionless form for four points near the fault plane, differing only in azimuthal angle. It may be seen that τ_{xz} has a rather different time history at each of the four azimuths, but the value for large times is everywhere the same, about -8 units. With an initial particle velocity of 100 cm per second, this translates to a stress drop of about 200 bars. Figure 4 differs from Figure 3 only in that the rupture velocities are halved. For the same initial particle velocity of 100 cm per second, the stress drop now is about 300 bars.

We should like to emphasize the three-dimensional nature of this earthquake model. Because the xz component of stress is the only component being relieved by fault motion, it follows that the other shear component on the fault plane, τ_{yz}, should have final values unchanged from zero. Figure 5 shows this indeed to be the case, in that τ_{yz} at different positions near the fault plane does tend to zero for large times, but it will be seen at intermediate values, particularly at times near the rupture arrival, to be large. This kind of feature is important to consider, since fault motions must begin at a point, and then spread over the fault surface with a rupture front which is a closed curve (or several closed curves) in the fault plane.

Figures 2, 3, 4 and 5 all describe the stress history near a rupturing fault and help us understand how stress is relieved by the stress relaxation phenomenon of the earthquake. But, of

course, seismic instruments are built typically to record acceleration, or displacement. Figure 6 shows both, again for four different azimuths, and plotted here as solid lines are the x components of acceleration and displacement, for points near the fault plane. The dashed line is the displacement time history for that point on the fault surface which is nearest the station with azimuthal angle as shown, and $\theta = 85°$. Acceleration clearly has a different time history at these locations, and if particle velocity is 100 cm per second on the fault, then maximum accelerations are around 1 g at the distance 10 km, for $\phi = 1°$, 30°, and 60°. The case $\phi = 89°$ is pathological, because there the rupture is essentially riding on the S wave wavefront, and accelerations are up around several tens of g, due to the Doppler focusing of energy. However, the displacement (obtained by double integration of acceleration) is about the same at all four different positions, and in each case the computed displacement is similar to the dashed curve, the actual shear dislocation of the nearest point on the fault surface.

Another displacement that is important to investigate is the component normal to the fault plane. Figure 7 shows the acceleration of displacement in this direction, in the case of somewhat slow rupture propagation. The first remarkable point is that the acceleration time history has essentially the same shape at all the four stations. However, the scale is very different. This similarity in shape is due to the fact that that part of the fault plane which is in motion has been twisted through a constant angle out of its original plane, so that the z components of acceleration and displacement will have a magnitude which is proportional to the

x coordinate. Displacement is shown here as a dashed line. The second important point to make is that the z displacement may be a good marker of the rupture front going nearby. If one actually had data for displacement of the type shown as dashed lines in Figure 7, then one would not be far wrong in picking the times of rapid change in z displacement as the time the rupture front is passing nearby.

The stress relaxation model being described in this section has the property of a stress drop which is proportional to particle velocity at the initial point of rupture. It is clearly useful to know the constant of proportionality, and in Figure 8a is plotted a value for this constant, for a range of rupture velocities. The solid curve in Figure 8a was attained by evaluating an integral given by Kostrov (1964), for a circular crack. Another way to get this curve is to take the time history of stress rate as shown in Figure 2 for a point near the fault plane, and to integrate this up to find the final static value of the stress drop. Carrying this procedure out at two different rupture speeds results in the two crosses shown on Figure 8a: the agreement with Kostrov's curve gives one confidence that the numerical work is self consistent. The basic observation to make about Figure 8a is that the curve is almost a straight line through the origin. In fact, the slight negative curvature is important , since it implies that faults are unlikely significantly to overshoot their final static displacement. One can conclude this by re-plotting the curve, using it to find out how much displacement there is at the center of the fault, at the time the fault surface has acquired a fixed

radius, e.g., 1 km. If rupture were then to stop, we ask: "Would displacement across the fault continue to grow in the same direction, or would it have to reverse?" The curve shown in Figure 8b indicates that if the fault displacements are to end up in a final static configuration which is appropriate to the stress drop prevailing during dynamic rupture, then the displacement will have to grow up to the static value from below, and overshooting is not required.

REFERENCES

Kostrov, B. V., Self-similar problems of propagating shear cracks, Journal of Applied Mathematics and Mechanics, 28, 1077-1087, 1964.

Richards, Paul G., The dynamic field of the growing plane elliptical shear crack, International Journal of Solids and Structures, 9, 843-861, 1973.

FIGURE CAPTIONS

Figure 1 Parameters for a growing elliptical crack: (a) the plane $z = 0$, seen from the side with $z > 0$; (b) the definition of spherical polar coordinates (R, θ, ϕ). Azimuth angle ϕ is taken between the plane $y = 0$, and the plane containing the field point and the z-axis.

Figure 2 The time history of stress rate, shown at four different azimuths. At bottom left is shown the relative positions of that part of the fault surface which is in motion (shown shaded); the S wave wavefront; and the P wave wavefront. Stress rate and time are plotted as dimensionless quantities, and factors shown at the upper right may be used to convert the plots to dimensioned values for specific cases.

Figure 3 As for Figure 4 but showing stress. This figure was obtained via a time integration of Figure 2.

Figure 4 As Figure 3, but with rupture speeds halved.

Figure 5 As Figure 3, but for the τ_{yz} component of shear.

Figure 6 As Figure 2, but showing the x-component of acceleration and displacement. Acceleration values are obtained from the peaked curves, and left-hand vertical scales: displacements from the monotonic curves, and right-hand scales. Dashed curves show the displacement time-history at nearest points on the fault surface itself.

Figure 7 As Figure 6, but for the slower rupture speeds, and the z-component of acceleration (solid) and displacement (dashed).

Figure 8 (a) Evaluation of formulae given by Kostrov (1964) for the particle velocity at fixed stress-drop, shown as a function of rupture speed, for a circular shear crack.

(b) Fault displacement (i.e., half the maximum offset), shown as a function of rupture speed, at the time the fault acquires a radius of 1 kilometer.

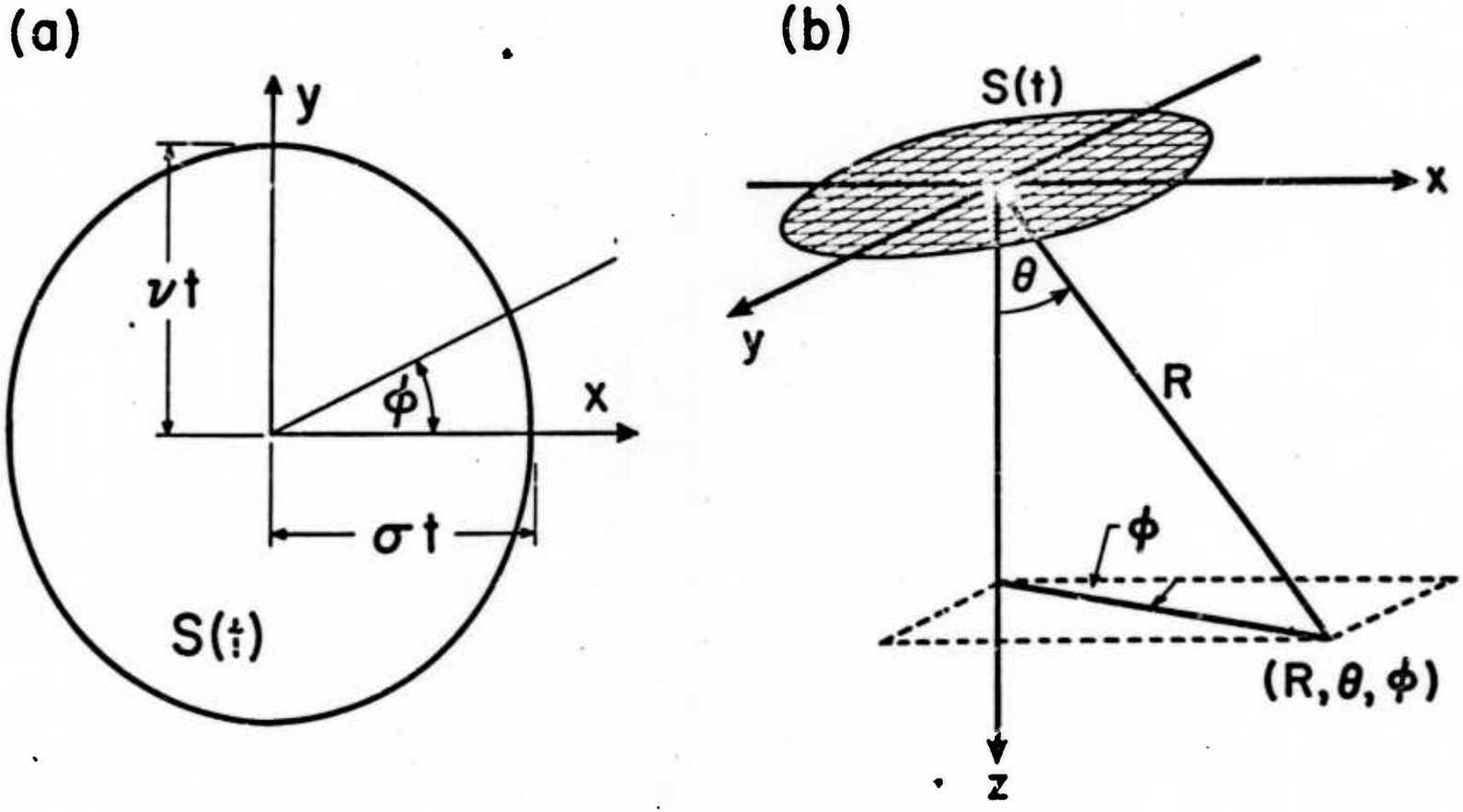

Figure 1

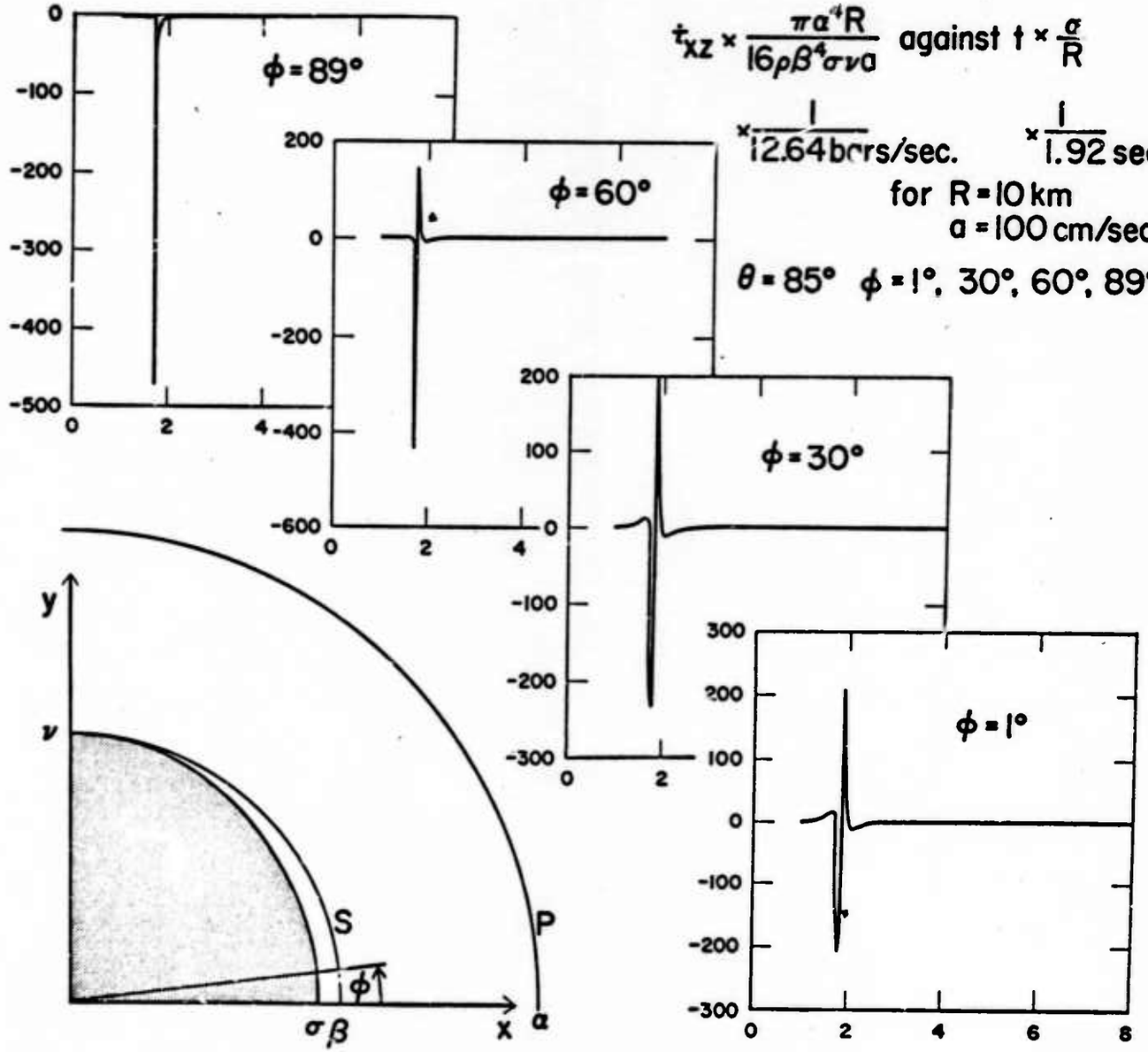
$t_{xz} \times \frac{\pi a^4 R}{16\rho\beta^4\sigma\nu a}$ against $t \times \frac{\sigma}{R}$
$\times \frac{1}{12.64 \text{ bars/sec.}}$
$\times \frac{1}{1.92 \text{ sec.}}$
for R = 10 km
a = 100 cm/sec.
θ = 85° φ = 1°, 30°, 60°, 89°
φ = 89°
φ = 60°
φ = 30°
φ = 1°
y
ν
S
P
φ
σβ
x
a
ν = β σ = 0.92ν

Figure 2

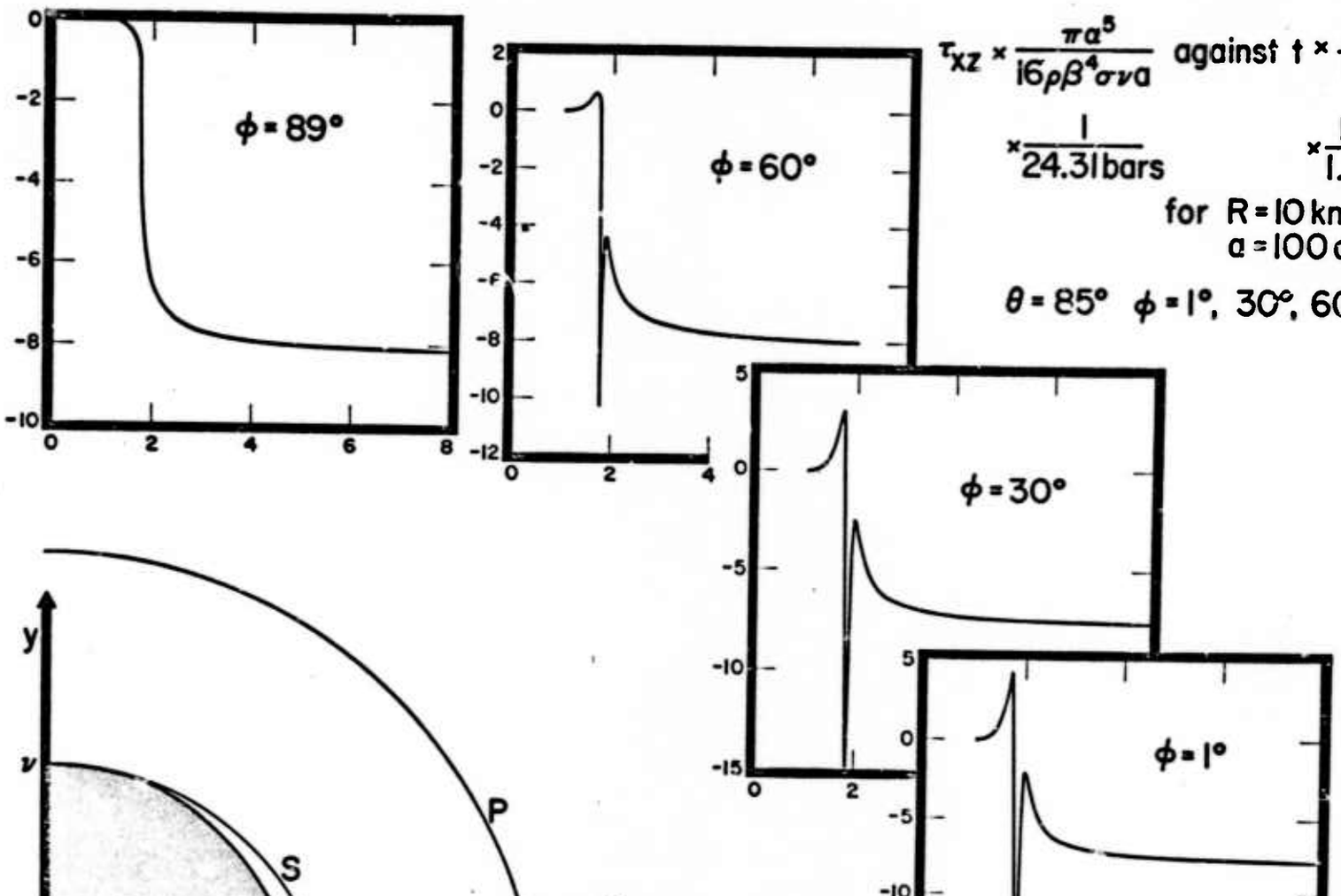
$\tau_{xz} \times \frac{\pi a^5}{16\rho\beta^4\sigma\nu a}$ against $t \times \frac{a}{R}$
$\times \frac{1}{24.31 \text{ bars}}$
$\times \frac{1}{1.92 \text{ sec.}}$
for R = 10 km
a = 100 cm/sec.
θ = 85° φ = 1°, 30°, 60°, 89°
φ = 89°
φ = 60°
φ = 30°
φ = 1°
y
ν
P
S
φ
σ β
x a
ν = β
σ = 0.92ν

Figure 3

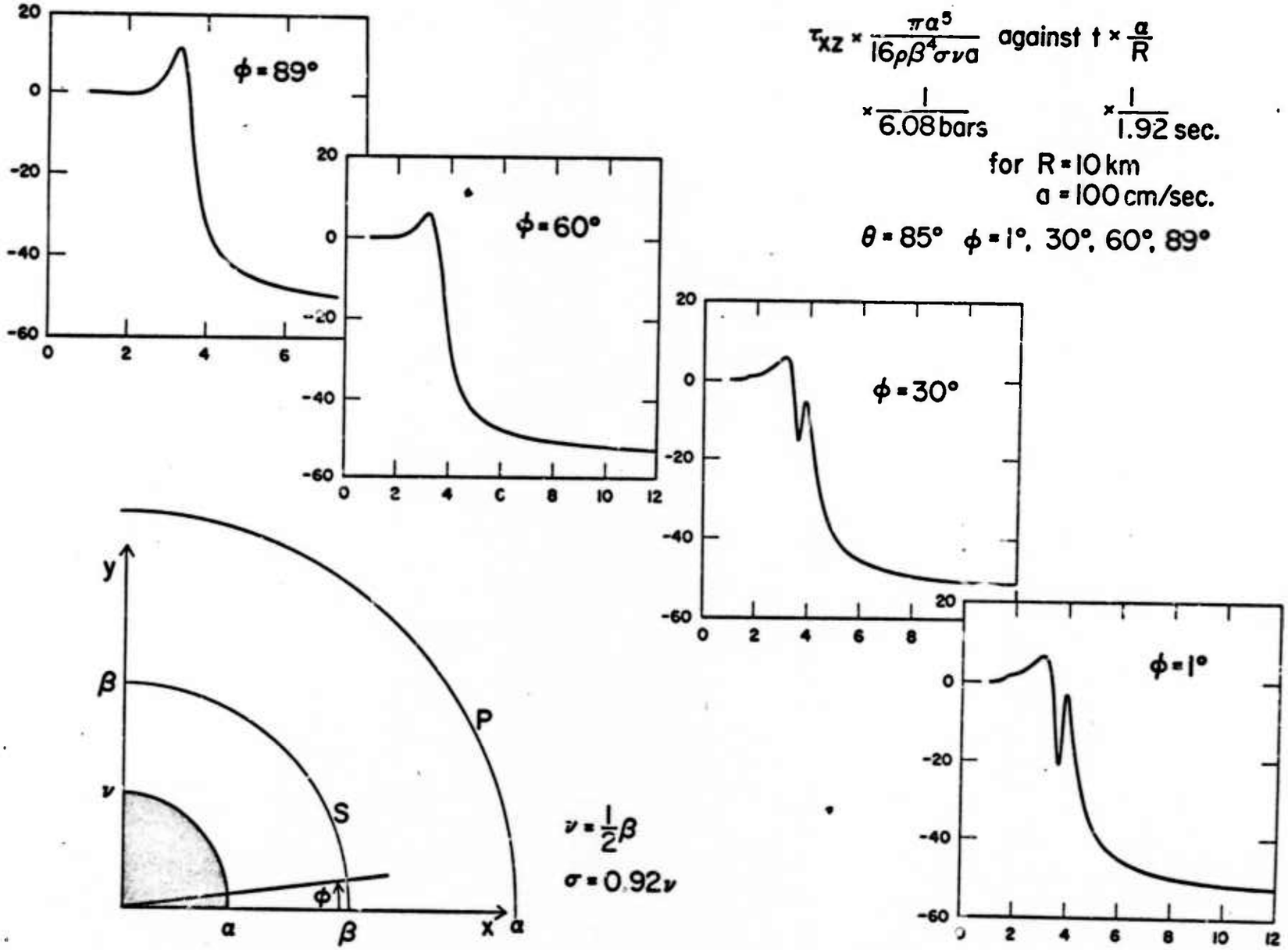
$\tau_{xz} \times \frac{\pi a^3}{16\rho\beta^4\sigma\nu a}$ against $t \times \frac{a}{R}$
$\times \frac{1}{6.08\,\text{bars}}$
$\times \frac{1}{1.92\,\text{sec.}}$
for R = 10 km
a = 100 cm/sec.
θ = 85° φ = 1°, 30°, 60°, 89°
φ = 89°
φ = 60°
φ = 30°
φ = 1°
y
β
ν
P
S
φ
α
β
x
α
$\nu = \frac{1}{2}\beta$
$\sigma = 0.92\nu$

Figure 4

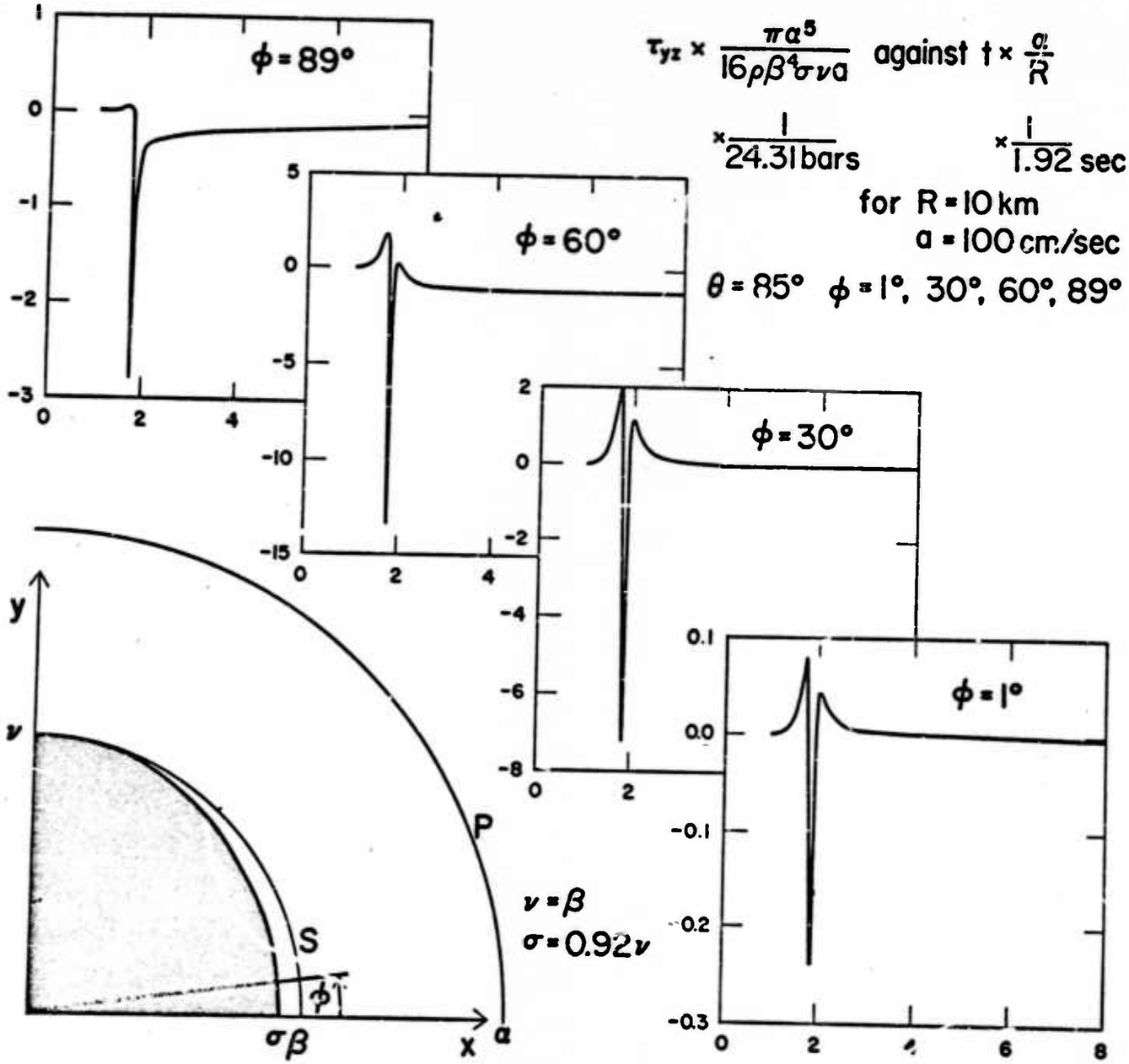
$\tau_{yz} \times \frac{\pi a^5}{16\rho\beta^4\sigma\nu a}$ against $t \times \frac{a}{R}$
$\times \frac{1}{24.31 \text{ bars}}$
$\times \frac{1}{1.92 \text{ sec}}$
for R = 10 km
a = 100 cm/sec
θ = 85° φ = 1°, 30°, 60°, 89°
φ = 89°
φ = 60°
φ = 30°
φ = 1°
y
ν
P
S
φ
σβ
x
a
ν = β
σ = 0.92ν

Figure 5

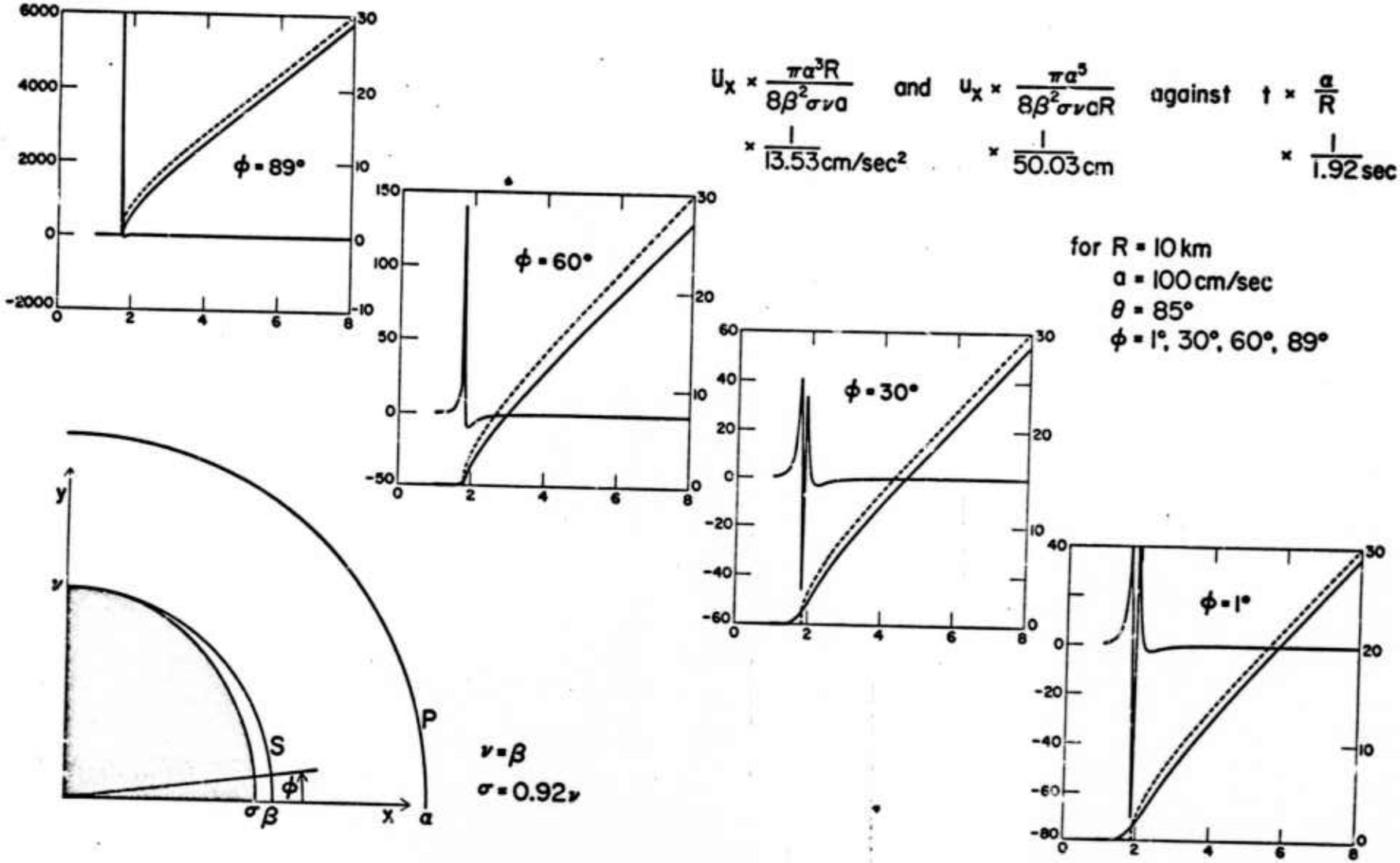
$U_x \times \frac{\pi\alpha^3 R}{8\beta^2\sigma\nu a}$ and $u_x \times \frac{\pi\alpha^3}{8\beta^2\sigma\nu cR}$ against $t \times \frac{a}{R}$
$\times \frac{1}{13.53\,cm/sec^2}$ $\times \frac{1}{50.03\,cm}$ $\times \frac{1}{1.92\,sec}$
for R = 10 km
a = 100 cm/sec
θ = 85°
φ = 1°, 30°, 60°, 89°
φ = 89°
φ = 60°
φ = 30°
φ = 1°
y
ν
S
P
σ β
φ
x
α
ν = β
σ = 0.92ν

Figure 6

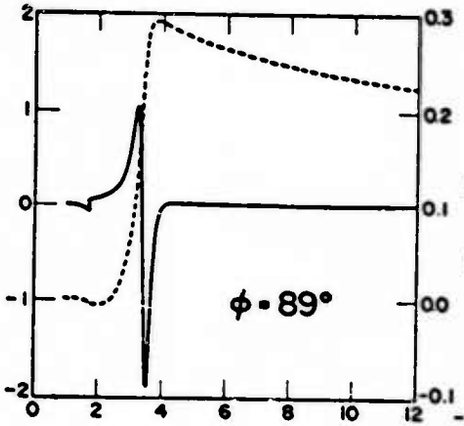

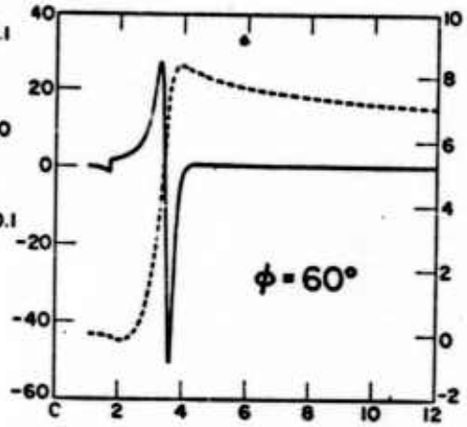

$\ddot{u}_z \times \frac{\pi a^3 R}{8\beta^2 \sigma \nu a}$ and $u_z \times \frac{\pi a^3}{8\beta^2 \sigma \nu a R}$ against $t \times \frac{a}{\beta^2}$

$\times \frac{1}{3.38\,\text{cm/sec}^2}$ $\times \frac{1}{12.51\,\text{cm}}$ $\times \frac{1}{1.92\,\text{sec}}$

for R = 10 km
a = 100 cm/sec
θ = 85°
ϕ = 1°, 30°, 60°, 89°

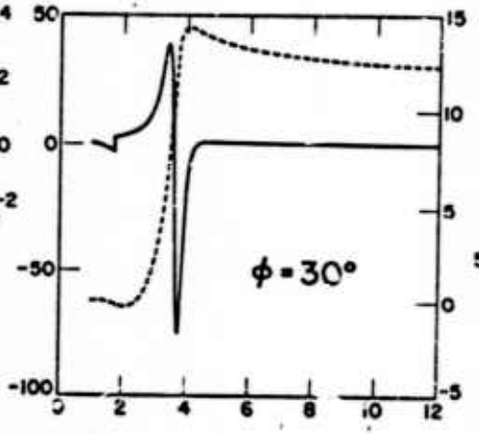

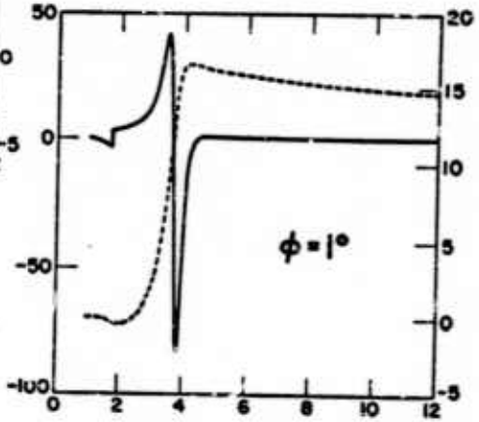

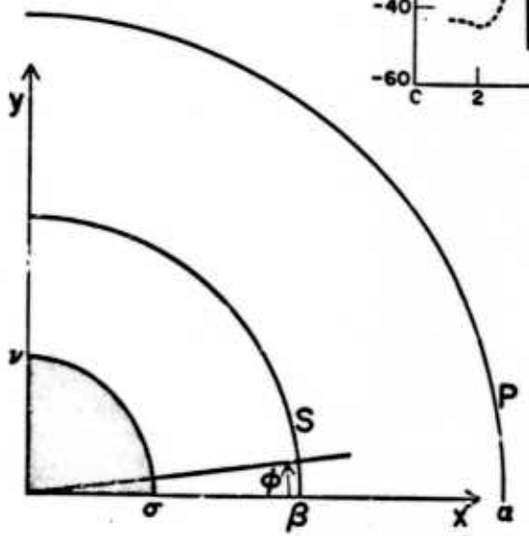

$\nu = \frac{1}{2}\beta$

$\sigma = 0.92\nu$

Figure 7

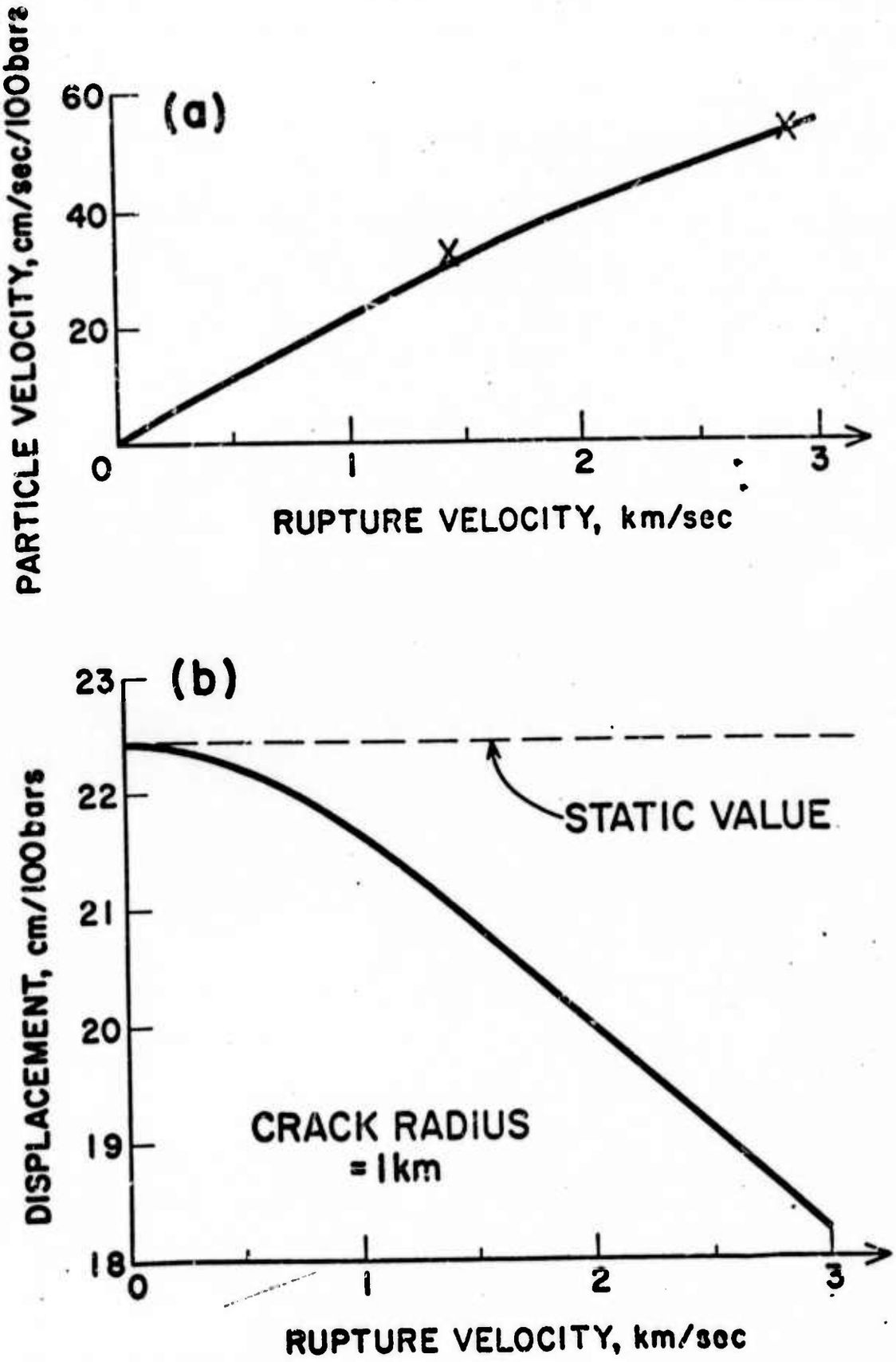
(a)
PARTICLE VELOCITY, cm/sec/100bars
60
40
20
0
1
2
3
RUPTURE VELOCITY, km/sec
(b)
DISPLACEMENT, cm/100bars
23
22
21
20
19
18
STATIC VALUE
CRACK RADIUS
= 1km
0
1
2
3
RUPTURE VELOCITY, km/sec

Figure 8

Program to Compute Seismograms from Prescribed Shear Dislocations: Comparison of Strong Ground Motion from Several Dislocation Models

One approach to studying details of the earthquake source mechanism is to study records of strong ground motion near the causative fault. At these short distances, where the effects of scattering and attenuation are minimal, one can best expect to learn about the way rupture grows and stops, and the time function of displacement on the fault. However, interpretation of strong motion accelerograms recorded near the causative fault is not straightforward. Several workers have studied these records in terms of a dislocation model in an infinite space. For the time history of dislocation, Aki (1968) used a propagating step, but later workers (for example, Haskell, 1969; Kanamori, 1972; Trifunac, 1974; Trifunac and Udwadia, 1974; Anderson, 1974) used a propagating ramp. These workers found particular combinations of parameters such that the displacements resulting from their models approximately fit the integrated accelerograms for the earthquakes studied. Their results demonstrate that the long period components of near field data can be fairly well matched, in spite of the limitations of the theory and the dislocation model.

Dislocation models are generally found by trial and error. The model found is not necessarily the best, nor is it the only one which will adequately fit the data. In fact, models significantly different from each other are possible. This ambiguity is demonstrated by the variety of solutions from several studies

of the Parkfield, California, earthquake of June 27, 1966. For example, models have been found with rupture velocities of 2.2 km/sec (Aki, 1968; Tsai and Patton, 1972), 2.4 to 2.5 km/sec (Trifunac and Udwadia, 1974) and 2.8 to 3.0 km/sec (Anderson, 1974).

In this paper the nature of this ambiguity is examined in more detail. This has been done in the following ways:

1) A computer program has been developed which can calculate, for a wide variety of dislocation models, the time history of displacement at any point in an infinite, homogeneous, elastic space.
2) Several types of dislocation models, including a propagating ramp, are used, and displacements at nearby stations are studied to try to learn: A) What factors of the fault motion are important to ground displacement nearby, and B) From the near ground displacement, how much can be learned about details of the fault dislocation.
3) Propagating ramp models permit relatively rapid computation, so we have used them in several cases to compare their near-field motions with those of other models. A surprisingly good match can often be found.
4) An attempt is made to understand why a propagating ramp can often work so well in fitting displacements caused by other dislocation models.

Description of Method

We model the earthquake by a discontinuity in displacement across a rupturing fault. Specifically:

1. A fault plane is assumed, here the $x_3 = 0$ plane. A location on the fault plane is given by $\vec{\xi} = (\xi_1, \xi_2)$. Station locations (observation points) are given as $\vec{x} = (x_1, x_2, x_3)$.
2. Here the fault will refer to that bounded region of the fault plane which is offset during the earthquake. During the earthquake, as viewed in inertial space, a particle at point $\vec{\xi}$ attached to the $x_3 > 0$ side of fault has the motion $\vec{u}^{+}(\vec{\xi}, t)$. If the same particle were attached to the $x_3 < 0$ side of fault, it would have the displacement $\vec{u}^{-}(\vec{\xi}, t)$. The dislocation function is then $\vec{D}(\vec{\xi}, t) = \vec{u}^{+}(\vec{\xi}, t) - \vec{u}^{-}(\vec{\xi}, t)$.
3. Using formulae given by Haskell (1969), the displacement at any point in an infinite homogeneous elastic space caused by the dislocation $\vec{D}(\vec{\xi}, t)$ can be calculated.

A computer program was developed which is capable of using any dislocation function $\vec{D}(\vec{\xi}, t)$ provided that function is smooth enough in space to be integrated using the ROMBERG scheme. This differs from the application usually made of Haskell's formula, in that we do not assume $\vec{D}$ to be the product of a function of space and a function of time. Furthermore, we do not restrict the time dependence to be ramplike. We do

however, require that the function be continuous in time. A typical formula from the Haskell paper is

$$u_1(\vec{x}, t) = (\beta^2/4\pi) \iint_\Sigma \gamma_3 \, 6(5\gamma_1^2-1)r^{-4} \int_{r/\alpha}^{r/\beta} D(\xi_1, \xi_2, t-t')t'dt'$$

$$+2(6\gamma_1^2-1)(\alpha r)^{-2} D(\xi_1, \xi_2, t-r/\alpha)$$

$$-3(4\gamma_1^2-1)(\beta r)^{-2} D(\xi_1, \xi_2, t-r/\beta)$$

$$+2\gamma_1^2(\alpha^3 r)^{-1} \dot{D}(\xi_1, \xi_2, t-r/\alpha)$$

$$\vdots$$

$$-(2\gamma_1^2-1)(\beta^3 r)^{-1} \dot{D}(\xi_1, \xi_2, t-r/\beta) \Big\} d\xi_1 d\xi_2$$

Here u_1 is the displacement in the x_1 direction due to a dislocation $\vec{D} = (D, 0, 0)$ on the fault plane Σ. Parameters α, β are the P- and S- wave velocities; $r = |\vec{x} - \vec{\xi}|$; and $\gamma_1 = (x_1 - \xi_1)/r$.

Integration of the terms in $\frac{\dot{D}}{r}$ were achieved by reversing the order of integration and differentiation as follows:

$$\iint_\Sigma \Big(2\gamma_3\gamma_1^2(\alpha^3 r)^{-1} \dot{D}(\xi_1, \xi_2, t-r/\alpha)$$

$$- \gamma_3(2\gamma_1^2-1)(\beta^3 r)^{-1} \dot{D}(\xi_1, \xi_2, t-r/\beta) \Big) d\xi_1 d\xi_2$$

$$= \frac{d}{dt} \iint_\Sigma \Big(2\gamma_3\gamma_1^2(\alpha^3 r)^{-1} D(\xi_1, \xi_2, t-r/\alpha)$$

$$- \gamma_3(2\gamma_1^2-1)(\beta^3 r)^{-1} D(\xi_1, \xi_2, t-r/\beta) \Big) d\xi_1 d\xi_2$$

For this step to be valid, it is usually sufficient that the dislocation function be continuous in time. This allows the

use of dislocation functions which have infinite particle velocities at the rupture front. The function which results from the double integration over the fault plane varies smoothly in time and does not cause any unusual problems in numerical differentiation.

All the integration is done using a ROMBERG scheme. The ROMBERG integrations were stopped when two successive estimates of the integral differed by less than a specified error, usually taken as 5%. At worst, the program took about 1½ sec/data point (3 displacement components for the same point in time) on an IBM 360-95, and at best was ten times faster.

The program was checked in the following ways:

1. Using a propagating ramp dislocation function, displacement seismograms were found to agree well with results of Tsai, Trifunac, and Boore (personal communications).
2. For several models, calculation of displacements at stations located on planes of symmetry resulted in displacement amplitudes (for theoretically zero components) at least five orders of magnitude smaller than for non-zero components.
3. Using a propagating ramp dislocation function, an array of 19 points in space for three times was found to yield a finite difference form of the elasticity equation:

$$\ddot{\vec{u}} = (\alpha^2 - \beta^2)\vec{\nabla}(\vec{\nabla}\cdot\vec{u}) + \beta^2\nabla^2\vec{u}$$

4. A severe test was made by taking the dislocation $\vec{D}$ to be that for a self similar crack, and comparing the calculated displacements with results obtained using an entirely different method (Richards, 1973).

The dislocation functions used here, which are intended to be illustrative and are not physically realistic, are given below. In Fig. 1, an example of all but one of the dislocation functions is given to show how it grows in space. The shading (see caption) denotes either that part of the fault which is in motion, or that part which has achieved less than half the final average offset. The symbol given for each dislocation model in Fig. 1, which schematically suggests the way the faults grow, will be used to identify models in later figures.

The self-similar crack is a solution (Burridge and Willis, 1969) for a crack growing in an infinite anisotropic elastic medium with constant tractions on the fault surface. To be useful for our purposes, there must also be a mechanism for stopping the rupture. Thus the dislocation function here called a "self-similar crack" is, initially, a self similar crack, but it is stopped instantaneously. The dislocation function called a "pinned annealing crack" also begins as a self-similar crack. When the rupture front reaches a designated point on the fault plane, that point does not rupture. From that point, an annealing front spreads which stops the rupture instantaneously as it passes other points on the fault.

The one source omitted from Fig. 1 is a smoothed propagating ramp with the time function suggested by Ohnaka (1973). For brevity we shall refer to this model as an "Ohnaka ramp". It is used as an example of a dislocation function in which the particle velocity on the fault is continuous in time. On Fig. 1, this model would look identical to the propagating ramp. Fig. 2 shows the dislocation function in time for three models, including the Ohnaka ramp which was omitted from Fig. 1.

For all the models given below, rupture begins at a point or on a line at $t = 0$, and a given point on the fault plane ruptures at $t = t_r(\xi_1, \xi_2)$. The dislocation direction is always parallel to ξ_1: $\vec{D} = (D, 0, 0)$.

The point $\vec{\xi} = (0, 0)$ is taken to be the geometrical center of the fault for all models except the pinned annealing crack, where it is the point rupture initiates.

Propagating Ramp

$$D = \begin{cases} 0 & |\xi_1| > L/2,\ |\xi_2| > W/2 \\ 0 & t \leq t_r \\ D_{max}\dfrac{t - t_r}{\tau} & t_r < t < t_r + \tau \\ D_{max} & t_r + \tau \leq t \end{cases}$$

where $$t_r = \frac{(\xi_1 + L/2)}{v}$$

Input:

- L = fault length
- W = fault width
- v = rupture velocity
- τ = rise time
- D_{max} = final displacement

Elliptic Propagating Ramp

$$D \begin{cases} 0 & \dfrac{\xi_1^2}{(L/2)^2} + \dfrac{\xi_2^2}{(W/2)^2} \geq 1 \\ 0 & t < t_r \\ D_{max}\dfrac{t - t_r}{\tau} & t_r < t < t_r + \tau \\ D_{max} & t_r + \tau < t \end{cases}$$

where $t_r = \dfrac{(\xi_1 + L/2)}{v}$

Input:
- L = fault length (length of axis of ellipse)
- W = fault width (length of axis of ellipse)
- v = rupture velocity
- τ = rise time
- D_{max} = final displacement

Self Similar Crack

$$D = \begin{cases} 0 & t_{max}^2 < \frac{\xi_1^2}{\sigma^2} + \frac{\xi_2^2}{\nu^2} \\ 0 & t < t_r \\ 2s\left(t^2 - \frac{\xi_1^2}{\sigma^2} - \frac{\xi_2^2}{\nu^2}\right)^{1/2} & t_r \leq t \leq t_{max} \\ 2s\left(t_{max}^2 - \frac{\xi_1^2}{\sigma^2} - \frac{\xi_2^2}{\nu^2}\right)^{1/2} & t_{max} < t \end{cases}$$

where $t_r = \left(\frac{\xi_1^2}{\sigma^2} + \frac{\xi_2^2}{\nu^2}\right)^{1/2}$

Input:
- σ = rupture velocity in ξ_1 direction
- ν = rupture velocity in ξ_2 direction
- s = particle velocity at origin
- t_{max} = time motion stops (instantly over entire fault)

Pinned Annealing Crack

$$D = \begin{cases} 0 & t_s(\xi_1, \xi_2) < \left(\frac{\xi_1^2}{\sigma^2} + \frac{\xi_2^2}{\nu^2}\right)^{1/2} \\ 0 & t < t_r \\ 2s\left(t^2 - \frac{\xi_1^2}{\sigma^2} - \frac{\xi_2^2}{\nu^2}\right)^{1/2} & t_r < t < t_s \\ 2s\left(t_s^2 - \frac{\xi_1^2}{\sigma^2} - \frac{\xi_2^2}{\nu^2}\right)^{1/2} & t_s < t \end{cases}$$

where
$$t_r = \left(\frac{\xi_1^2}{\sigma^2} + \frac{\xi_2^2}{\nu^2}\right)^{1/2}$$
$$t_s = t_a + \frac{r_a}{c}$$
$$t_a = \left(\frac{a_1^2}{\sigma^2} + \frac{a_2^2}{\nu^2}\right)^{1/2}$$
$$r_a = \left((\xi_1 - a_1)^2 + (\xi_2 - a_2)^2\right)^{1/2}$$

Input:
- σ = rupture velocity in ξ_1 direction
- ν = rupture velocity in ξ_2 direction
- s = particle velocity at origin
- (a_1, a_2) = point on fault where annealing begins
- c = annealing velocity

Bilateral Propagating Ramp

$$D = \begin{cases} 0 & |\xi_1| > L/2,\ |\xi_2| > W/2 \\ 0 & t \leq t_r \\ D_{max}\dfrac{t - t_r}{\tau} & t_r < t < t_r + \tau \\ D_{max} & t_r + \tau \leq t \end{cases}$$

where $t_r = \dfrac{|\xi_1|}{v}$

Input:

- L = fault length
- W = fault width
- v = rupture velocity
- τ = rise time
- D_{max} = final displacement

Ohnaka Ramp

$$D = \begin{cases} 0 & |\xi_1| > L/2,\ |\xi_2| > W/2 \\ 0 & t < t_r \\ D_{max}\left[1 - \left(1 + \dfrac{t - t_r}{\tau_0}\right)\exp\left(-\dfrac{t - t_r}{\tau_0}\right)\right] & t_r < t < t_r + 10\tau_0 \\ D_{max} & t_r + 10\tau_0 < t \end{cases}$$

where $t_r = \dfrac{(\xi_1 + L/2)}{v}$

Input:

- L = fault length
- W = rupture velocity
- v = rupture velocity
- τ_0 = related to rise time
- D_{max} = final displacement

Numerical Results

To permit meaningful comparisons between different models, two normalizations are used through the rest of this paper, unless specifically noted otherwise. First, we take the fault area $A = 1\ km^2$. This fault area might be in the range appropriate for a magnitude 2½ to 3 earthquake (Wyss and Brune, 1968). Second, we note from equation (1) and from Haskell (1969) that the displacement at the station is linearly proportional to the displacement on the fault surface. Therefore, without loss of generality we take the average displacement on the fault to be $\bar{u} = 1$ cm. The displacements calculated are plotted as the fraction of the average displacement on the fault. Unless noted otherwise, the station is a distance 1 km from the center of the fault, but may be considerably closer to some portion of the fault.

In what follows, all the above dislocation functions will be used to calculate displacements at several stations. When comparing faults with different geometry, the parameters are chosen and the final faults aligned so the models will have as much of the fault plane in common as possible. The location of all the stations used are listed in Table 1. We will be examining the derived displacements, and comparing to see what can be learned about the source model. The crucial point in examining the differences between two seismograms is to see if those differences are large enough to make

it possible to distinguish between the two source models. In many cases, we find two different source models are indistinguishable, in that their near field motions differ by less than the uncertainty found in comparable real data.

Fig. 3 shows the results of calculations for three different models of propagating ramps. The three models are

1. a starting model of v = 3.0 km/sec, τ = 0.12 sec,
2. a model where τ has been decreased to 0.0455 sec,
3. a model with the lower value of τ, and where the rupture velocity has been decreased to 2.5 km/sec.

It is seen in Fig. 3a that models (1) and (3) look remarkably similar. Fig. 3b shows results of the same models at another station, with the same results. These figures illustrate the important point that, when a propagating ramp is chosen to fit a displacement record, the choices of rupture velocity and rise time can be traded off.

It is interesting for these propagating ramp models to compare the total time required for rupture. We designate as T_r the total time interval during which the fault is rupturing. For a propagating ramp, $T_r = L/v + \tau$. For the cases shown in Fig. 3a and 3b,

1. $T_r = \frac{0.968}{3.0} + 0.12 = .443$ sec.
2. $T_r = \frac{0.968}{3.0} + 0.0455 = .368$ sec.
3. $T_r = \frac{0.968}{2.5} + 0.0455 = .433$ sec.

For the cases which resemble each other closely, T_r differs

by about 2%. For the cases which appear significantly different, T_r differs by about 20%. This suggests that T_r is an important parameter in controlling strong motion near a fault. To investigate this further, additional cases were run. For each of these cases, two propagating ramp models were chosen such that the rupture velocities differed substantially but T_r was the same. In Fig. 3c, the displacements are shown at seven stations representing several azimuths from the center of the fault. Thus we are testing whether the agreement in Figs. 3a and 3b is a result of the choice of stations. It can be seen that the waveform varies strongly with azimuth where the rupture is propagating toward the station, but fairly weakly with azimuth at back angles. However, at each station, the two propagating ramps generate similar waveforms. This figure, therefore, indicates that the ambiguity of rupture velocity and rise time observed in Figs. 3a and 3b was not peculiar to the choice of station.

For Fig. 3d, the same rupture models were used as for Fig. 3c, but the station is 4 km from the center of the fault. The station is near nodal for P-waves. The strong S-wave pulses from the two models are quite similar. This example suggests that within the near field the ambiguity is not sensitive to the distance between the fault and the station.

For Fig. 3e, rather than a nearly square rupture, the fault has L = 2.5 km and W = 0.4 km. Again, with rupture toward the station, and T_r the same for the two models, the displacements derived from the two models are remarkably similar.

In Figs. 4-6, we show the results of computations to examine other aspects of rupture for models which are basically unilateral. The parameter T_r is similar for models being compared in nearly all following figures.

Figs. 4a and 4b show the comparison of a propagating ramp and an Ohnaka ramp. At the two stations considered, the displacements resulting from the two dislocation functions are almost indistinguishable.

Next we consider three rupture models with slightly differing fault surfaces. Fig. 5 shows the faults used for a propagating ramp, elliptical propagating ramp, and a pinned annealing crack. Fig. 6 shows the resulting displacement seismograms for one station near the initiation of rupture (Fig. 6c) and two near where it finally ceases (Figs. 6a, 6b). For this and later figures where the epicenters of the models are not the same, we have shifted some of the models slightly along the time axis. The effect of this shift is to have the rupture (or in one case later the stopping) occurring at about the same time and place for all models. Apparently the effect of the shape of the fault is not of major importance, since the two ramps, with identical dislocation functions, differ only slightly. The models show the greatest differences near where the rupture ceases.

The difference between the propagating ramp and the pinned annealing crack appears to be of the nature that can be compensated by a decreased rupture velocity or increased rise

time in the propagating ramp, as in Figs. 3a, 3b. However, continued searches showed that the propagating ramp parameters used in Fig. 6 cannot be substantially improved upon, within the constraint that the average displacement be 1 cm. The differences appear to arise from the very high particle velocities on the fault surface of the pinned annealing crack. Since the amplitude of far-field (1/r) radiation from a fault element is proportional to the particle velocity on that fault element, there is very high radiation from the crack tip. In fitting with a propagating ramp model, this may result in assigning a larger average displacement to the fault surface than actually occurred.

So far, then, we have examined four models of rupture which are predominantly unilateral in nature. It appears that at least at these distances, and for the fault sizes chosen, the particle motion would be very difficult to learn from displacement records of the earthquake. The addition of new stations at the same distance provides little new information.

We now turn our attention to two basically bilateral source functions and begin by comparing a bilateral propagating ramp with a unilateral propagating ramp having the same geometry. At the station shown in Fig. 7 there are substantial differences in the u_3 component which would be sufficient to distinguish between the two models. In Fig. 8, however, a bilateral model with $v = 3.0$ is compared with a unilateral model with

$v = 6.0$. The rise times are the same. Thus T_r is identical for the two models. The differences at the station chosen in Fig. 8a are small. Where the unilateral model is not propagating predominantly toward the station, the two models differ substantially, as shown in Figs. 8b, 8c. Thus addition of new stations helps distinguish between unilateral and bilateral rupture. This suggests that the predominant direction or directions of rupture propagation is important in determining strong motion in the near field.

Fig. 9 compares a self similar crack model, which grows radially, with a bilateral propagating ramp. The bilateral crack grows with the same propagation velocity (in the ξ_1 direction) as the self similar crack. These cracks grow and stop in very different ways, but the predominant direction of rupture growth is similar to the extent that rupture initiates on a point or a line through the center of the fault. Fig. 9 shows differences in the resulting near-field displacements. However, these differences are perhaps not as great as one would have expected, for such different fault models.

Although most models of a unilateral ramp show little resemblance to a self-similar crack, one interesting comparison can be made. This is shown in Fig. 10. A propagating ramp is used with a propagation velocity of 100 km/sec, so that the entire fault starts and stops nearly instantaneously. There are substantial differences at the beginning of the records, reflecting the different way in which the dislocations

begin. But the strong resemblance of the two events at the end of the records reflects that they stopped in a nearly identical fashion.

The previous figures have not shown a particularly encouraging situation for the goal of identifying details of the rupture process from the displacement near the fault. It is possible that this is due, in part, to the particular dimensions chosen in the normalization described earlier. All the earthquakes shown so far would probably correspond to magnitude around 2½ to 3. Certainly as the station is moved closer to the fault plane, displacement there would more closely resemble the displacement dislocation function for that part of the fault. One would also expect that, if the station were kept the same absolute distance from the fault, then for a larger earthquake, represented by a larger fault plane, the displacement at the station would more closely resemble the fault dislocation. We, therefore, imagine a strike slip geometry with a station located on the ground surface for earthquakes with fault area 12.6 km^2, 70.8 km^2 and 402.0 km^2. For convenience, we will label these by magnitude 4, 5, and 7, respectively, although these fault areas are smaller than the areas predicted for earthquakes of such magnitudes by the formula of Wyss and Brune (1968). In increasing the fault areas, we take the predominant increase to be in the length. As a result, the length of the "magnitude 7" earthquake (L = 67 km) is comparable to the length of the fault trace

developed for the May 18, 1940, Imperial Valley, California, earthquake, which had a magnitude 7.1 (Richter, 1958). The stations are a distance 5 km from the center of the faults, thus slightly over one fault length for the "magnitude 4" earthquake. We pose the question of whether one could distinguish between a propagating ramp and an Ohnaka ramp. Results of these calculations are shown in Figs. 11a, 11b, 11c. The two source time functions give larger differences for all three cases than they did for the smaller fault in Figs. 4a, 4b. Nevertheless, it is not clear that a distinction could be made in any of these cases, using data with possible noise and unknown surface effects. The components not parallel to the direction of dislocation show possibly important differences, while the component parallel to the dislocation does not.

Discussion

So far we have seen that a considerable variety of dislocation functions and parameters can be used to give basically similar wave forms at stations near a moving fault. Some understanding of this similarity can be obtained by examination of the Fourier amplitude spectrum of one of the cases. This is shown in Fig. 12 for one of the propagating ramp models shown in Fig. 3b. It should be noted that this Fourier amplitude spectrum is not comparable to the spectra which are most often seen in connection with source studies. There are two important differences. First, it is a near field spectrum rather than far field. It, therefore, behaves as ω^{-1} at long periods due to the permanent offset. Second, the P- and S-waves are not separated, and the spectrum includes both.

In Fig. 12 the displacement spectral density decreases rapidly to 25 Hz, then begins to rise again. This rise is due to the small errors involved in the calculation of displacement. The frequency where it appears is correlated approximately with the average spacing of integration points on the fault and it can be adjusted through the error limit specified in the calculation.

If any corners exist in the spectrum, one might expect them to correlate with times characteristic of the source function. The rupture front crosses the fault in 0.4 sec, corresponding to a frequency of 2.5 Hz. The rise time is 0.0455 sec corresponding to a frequency of about 22 Hz. If one assiduously searches the spectrum for corners, they might be found indicated at 3.5 Hz and 12 Hz, with a fall-off of ω^{-4} after the second one. The important point is that before the emergence of numerical noise, the spectral amplitude is decreasing very rapidly with increasing frequency. The high frequencies which are needed to examine details of the faulting, such as how the rupture starts, were not reached in this calculation with assigned error of one-tenth normal, or one-half percent. These frequencies would be very weakly represented in a record of displacement, even when calculated with high accuracy.

Clearly it would be advantageous to study the acceleration instead of the displacement. Since this has the effect of

multiplying the amplitude spectrum by ω^2 the acceleration response would approximately be flat, to about 20 Hz. Moreover, near-field data is usually gathered in terms of acceleration. Unfortunately, to achieve the needed accuracy for two numerical differentiations (as was done in the test for obeying the wave equation) one requires at least a ten-fold increase in computation time.

It is not at all clear whether calculations of accelerations are justified. Effects due to the free surface and due to layering can be expected to be large at higher frequencies. Therefore, a dislocation model formulated for an infinite space would be of questionable value in any comparison with data at other than long periods. This suggests that a dislocation model, as used here, is not appropriate for learning about the details of rupture. This does not modify its usefulness in studying the gross features of rupture, as has been done for the Parkfield and San Fernando earthquakes in the studies mentioned earlier.

An examination of the displacements in Figs. 3-11 will show that in many cases, for large and small earthquakes, the component of motion parallel to displacement on the fault (u_1) is the least useful in distinguishing between different dislocations. The component perpendicular to the fault plane tends to be the most sensitive to choice of model.

Conclusions

There is considerable ambiguity in using near-field displacements to determine parameters of a dislocation model for an earthquake. One fault length from the center of small faults, one can determine quite well the total time spent in rupture. With more than one station, one can also determine the predominant direction(s) of rupture growth. However, with the exception of very high particle velocities on the fault surface, details of the time function or the fault shape have relatively little influence on the displacements at near-field stations.

References

Aki, K., 1968. Seismic displacements near a fault, J. Geophys. Res., 73, 5359-5376.

Anderson, J., 1974. A dislocation model for the Parkfield earthquake, Bull. Seis. Soc. Am., 64, 671-686.

Burridge, R. and J. R. Willis, 1969. The self-similar problem of the expanding elliptical crack in an anisotropic solid, Proc. Cambridge Phil. Soc., 66, 443-468.

Haskell, N. A., 1969. Elastic displacement in the near field of a propagating fault, Bull. Seis. Soc. Am., 59, 865-908.

Kanamori, H., 1972. Determination of effective tectonic stress associated with earthquake faulting. The Tottori earthquake of 1943, Phys. Earth and Planet. Interiors, 5, 426-

Ohnaka, M., 1973. A physical understanding of the earthquake source mechanism, J. Phys. Earth, 21, 39-59.

Richards, P. G., 1973. The dynamic field of a growing plane elliptical shear crack, Int. J. Solids Structures, 9, 843-861.

Richter, C. F., 1958. Elementary Seismology, W. H. Freeman & Co., San Francisco.

Trifunac, M. D., 1974. A three dimensional dislocation model for the San Fernando, California, earthquake of February 9, 1971, Bull. Seis. Soc. Am., 64, 149-172

Trifunac, M. D. and F. E. Udwadia, 1974. Parkfield, California earthquake of June 27, 1966: A three dimensional moving dislocation, Bull. Seis. Soc. Am., 64, 511-533.

Tsai, Y. B. and H. J. Patton (1972). Near field small earthquakes - dislocation motion. Semi annual technical report No. 1, 1 May 1972 to 31 Oct. 1972. Texas Instruments, Incorporated, Services Group.

Wyss, M. and J. N. Brune, 1968. Seismic moment, stress, and source dimensions for earthquakes in the California-Nevada region, J. Geophys. Res., 73, 4681-4694.

Table 1

Station Locations

No.	x_1(km)	x_2(km)	x_3(km)
1	0.863	-0.500	0.075
2	0.750	-0.500	0.433
3	0.433	-0.500	0.750
4	0.0	-0.500	0.866
5	-0.433	-0.500	0.750
6	-0.750	-0.500	0.433
7	-0.863	-0.500	0.075
8	0.837	-0.500	0.224
9	-0.837	-0.500	0.224
10	3.954	-0.500	0.346
11	0.0	4.0	3.0

Figure Captions

Fig. 1. Growth of crack models in time. Solid lines outline the area ruptured at each of the times shown. Broken lines are healing fronts, separating areas which have ceased motion from areas which are still moving. Names by which these models are referred to are: 1) propagating ramp, 2) elliptical propagating ramp, 3) self similar crack, 4) pinned annealing crack, 5) bilateral propagating ramp. For the ramp models the shaded areas are in motion. For the other two models, a shaded point has achieved less than one-half the final average displacement of the fault regardless of whether it is stopped or moving. The symbol above each model will be used to identify the model in all later figures.

Fig. 2 Particle motion on the fault with time. To the left, for each of three models, is an outline of the final fault shape. To the right is the time history of particle motion for particles on the fault, at positions indicated by the beginning level of the lines. The central model, indicated by a new symbol in this figure, is a propagating ramp with an Ohnaka time function (see text). For the pinned annealing crack at right only, the time functions apply only to the midline of the fault. The horizontal (time) and vertical (displacement) scales are arbitrary.

Fig. 3a. Effect of varying the rupture velocity and rise time for a propagating ramp. The rupture velocity and rise time for each model is given in the upper right corner. Parameters common to all models are L = 0.968 km, W = 1.032 km, D_{max} = 1.0 cm. In the box at lower right, two views of the fault are given, showing the fault and station projected onto the x_1 - x_3 plane and the x_1 - x_2 plane, the station is no. 2 in Table 1. For the view in the x_1 - x_3 plane, looking in the $+x_2$ direction. The arrows indicate that the offset is left lateral. Fault growth is in the same sense as in Fig. 1, i.e., here rupture initiates at the left and crosses the fault to the right. The two vertical lines next to the fault views show the distance, on the same scale, which would be traveled by a P-wave (α = 6.0 km/sec) and an S-wave (β = 3.4 km/sec) in one time unit. The lines labelled u_1, u_2, u_3 give the displacements in the x_1, x_2, x_3 directions at the station shown in the box. The vertical scale is the fraction of the average displacement on the fault plane.

Fig. 3b. Model same as Fig. 3a, at station location No. 3.

Fig. 3c. Comparison at seven stations of displacements from two propagating ramp models with the same T_r. For both models, L = 1.0 km, W = 1.0 km, D_{max} = 1.0 cm. The rupture velocities and rise times are indicated. The numbers beside the stations refer to the station number in Table 1.

Fig. 3d. Comparison of the models in Fig. 3c at station 10, 4.0 km from the center of the fault.

Fig. 3e. Comparison of two long, narrow propagating ramps with identical T_r. Model parameters are L = 2.5 km, W = 0.4 km, D_{max} = 1.0 cm. Rupture velocity (in km/sec) and rise time (in sec) for each model is shown in the figure Station No. 8. For explanation of other symbols, see Fig. 3a.

Fig. 4a,b. Comparison of propagating ramps with a linear and a smoothed time function at Station No. 2 (4a) and 3 (4b). Model parameters are L = 0.968 km, W = 1.032 km, v = 3.0 km/sec, D_{max} = 1.0 cm for both models. For the linear time function, τ = 0.12 sec, and for the Ohnaka time function τ_0 = 0.03 sec. For explanation of other symbols, see Fig. 3a.

Fig. 5. Comparison of the fault rupture areas of the models in Figs. 6. The three stations used are shown projected onto the fault plane. Arrows point to where rupture initiates.

Fig. 6a,b,c. Comparison of three faulting models at three stations. Parameters for the models are the following: Propagating ramp: L = 2.31 km, W = 0.43 km, v = 3.0 km/sec, τ = 0.045 sec, D_{max} = 1.0 cm. Elliptical propagating ramp: L = 2.60 km, W = 0.49 km, v = 3.0 km/sec, τ = 0.05 sec, D_{max} = 1.0 cm. Pinned annealing crack: s = 6.17 cm/sec, σ = 2.7 km/sec, ν = 1.0 km/sec, a_1 = -0.191 km, a_2 = 0.0 km, c = 3.2 km/sec. Stations are No. 8 (6a), No. 2 (6b), and No. 9 (6c). For explanation of other symbols, see Fig. 3a.

Fig. 7. Comparison of a unilateral and a bilateral faulting model. For both models, L = 1.0 km W = 1.0 km, v = 2.5 km/sec, τ = 0.05 sec, D_{max} = 1.0 cm Station No. 2. For explanation of other symbols, see Fig. 3a.

Fig. 8a,b,c. Comparison of a unilateral and a bilateral faulting model at two stations. For both models, L = 1.0 km, W = 1.0 km, τ = 0.2 sec, D_{max} = 1.0 cm. For the bilateral model, v = 3.0 km/sec, and for the unilateral model, v = 6.0 km/sec. Stations are No. 2 (8a), No. 9 (8b), and No. 4 (8c). For explanation of other symbols, see Fig. 3a.

Fig. 9a,b,c. Comparison of a bilateral and a self similar crack model at three stations. For the bilateral crack, L = 1.0 km, W = 1.0 km, v = 3.0 km/sec, τ = 0.05 sec, D_{max} = 1.0 cm; for the self similar crack, s = 4.125 cm/sec, σ = 3.0 km/sec, ν = 3.2 km/sec, t_{max} = 0.182 sec. Stations are No. 2 (9a), No. 3 (9b), and 4 (9c). For explanation of other symbols, see Fig. 3a.

Fig. 10a,b,c. Comparison of a self similar crack and a propagating ramp which stops similarly. For the self similar crack, s = 4.125 cm/sec, σ = 3.0 km/sec, ν = 3.2 km/sec, t_{max} = 0.182 sec; for the propagating ramp, L = 0.968 km, W = 1.032 km, v = 100.0 km/sec, τ = 0.182 sec, D_{max} = 1.0 cm. Stations are No. 2 (10a), No. 3 (10b), and No. 4 (10c). For explanation of other symbols, see Fig. 3a.

Fig. 11a. Comparison of propagating ramps with linear and smoothed time functions. The parameters might be appropriate to an earthquake of magnitude about 4. For both models, L = 3.55 km, W = 3.55 km, v = 3.0 km, D_{max} = 1.0 cm. For the linear ramp, τ = 2.5 sec. For the smoothed ramp, τ_0 = 0.625 sec. In this case, the station No. 11 is a distance 5.0 km from the center of the fault. For explanation of other symbols, see Fig. 3a.

Fig. 11b. A "magnitude 5" earthquake. For both models, L = 11.8 km, W = 6.0 km, v = 3.0 km/sec, D_{max} = 1.0 cm. For the linear ramp, τ = 5.0 sec. For the smoothed ramp, τ_0 = 1.25 sec. Station No. 11.

Fig. 11c. A "magnitude 7" earthquake. For both models L = 67.0 km, W = 6.0 km, v = 3.0 km/sec, D_{max} = 1.0 cm. For the linear ramp, τ = 5.0 sec. For the smoothed ramp, τ_0 = 1.25 sec. Station No. 11.

Fig. 12. Fourier Displacement spectral amplitude for one of the models shown in Fig. 3b. This is the spectrum of near field displacement, so the long period limit should be as ω^{-1}. Note that the spectrum contains both P- and S-waves.

5
4
3
2
1
0.0+
0.2
0.4
0.6
0.8
1.0

2

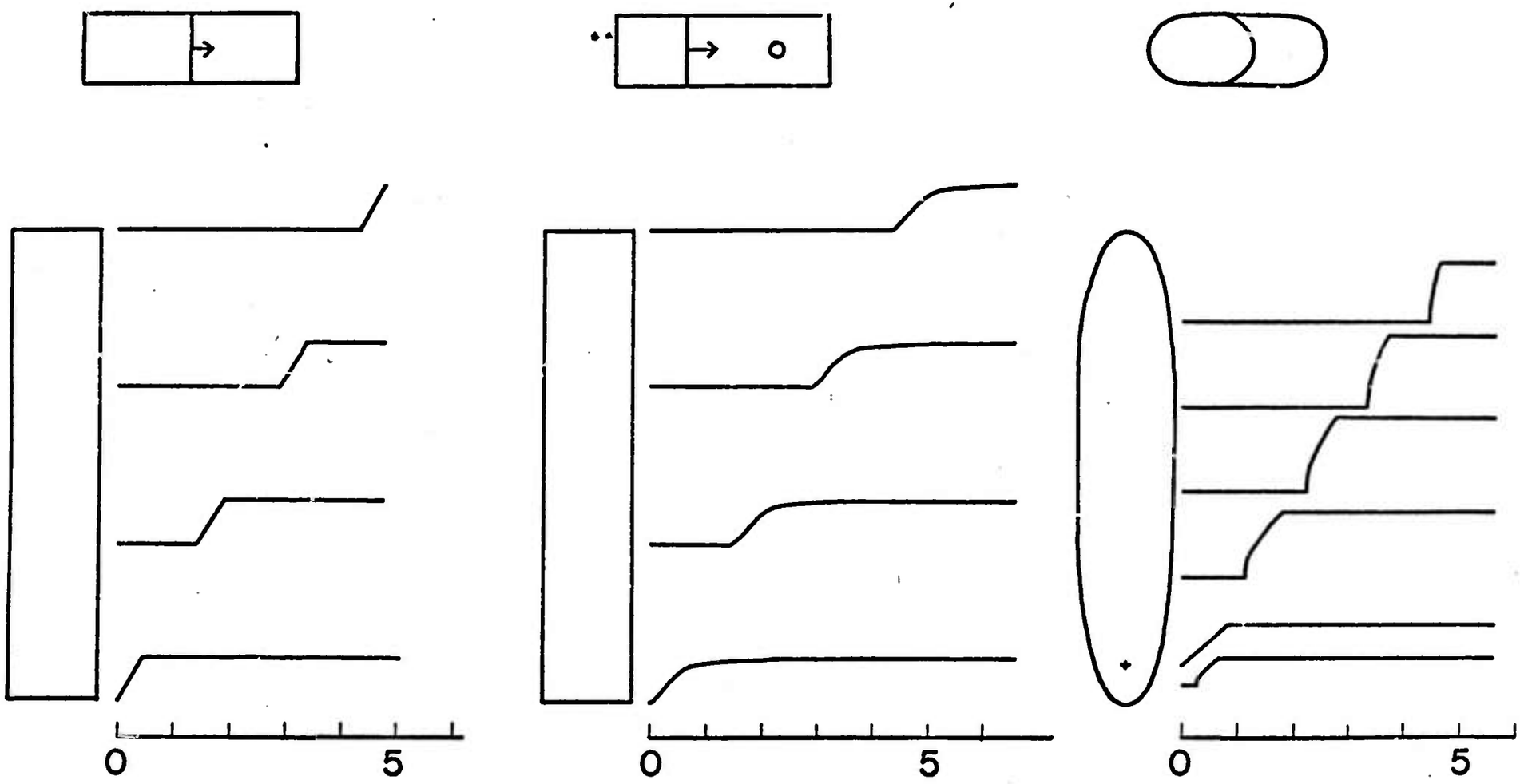

45

3a

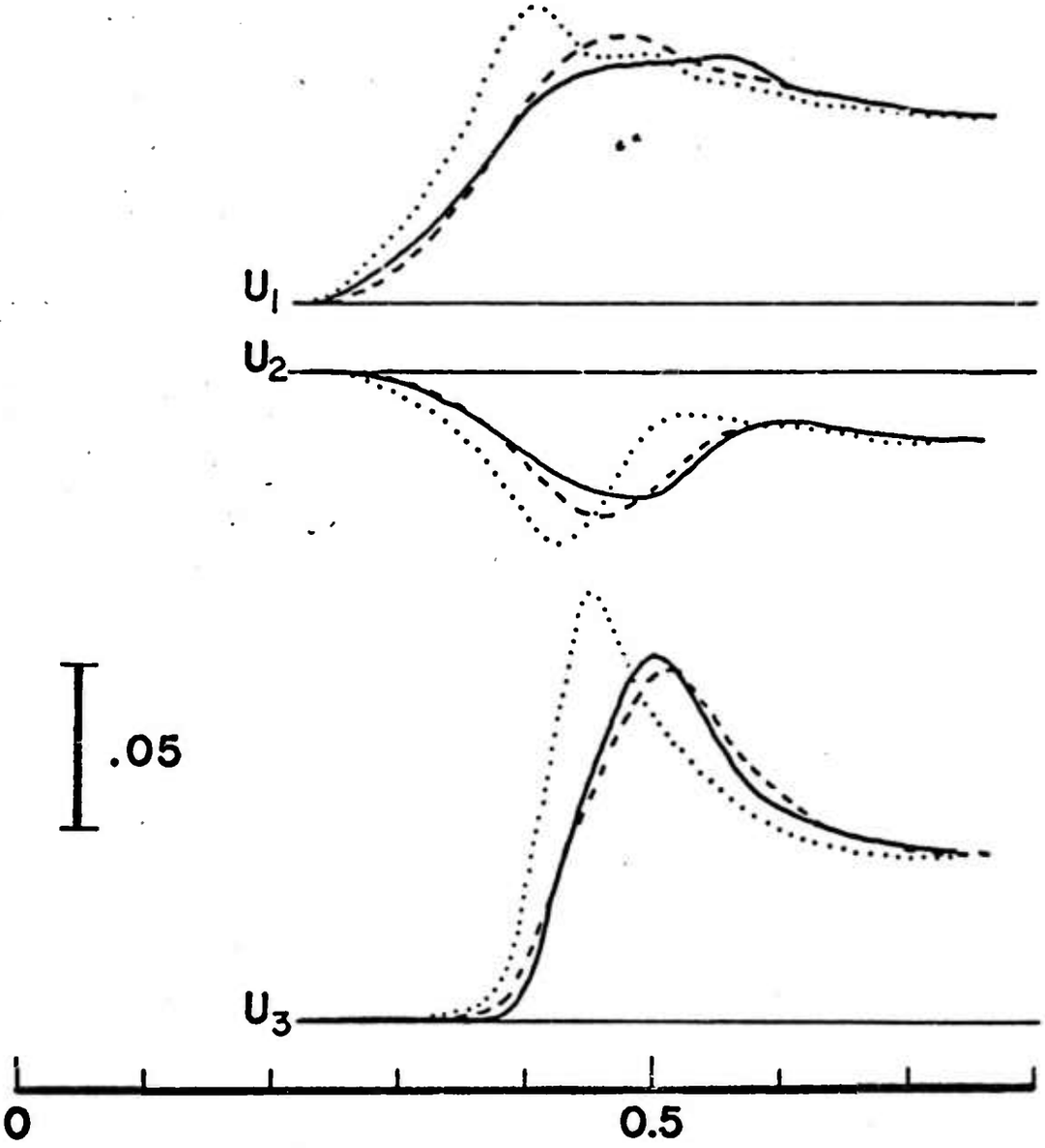

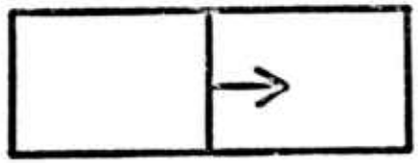

	V	τ
---	3.0	0.12
·····	3.0	0.0455
——	2.5	0.0455

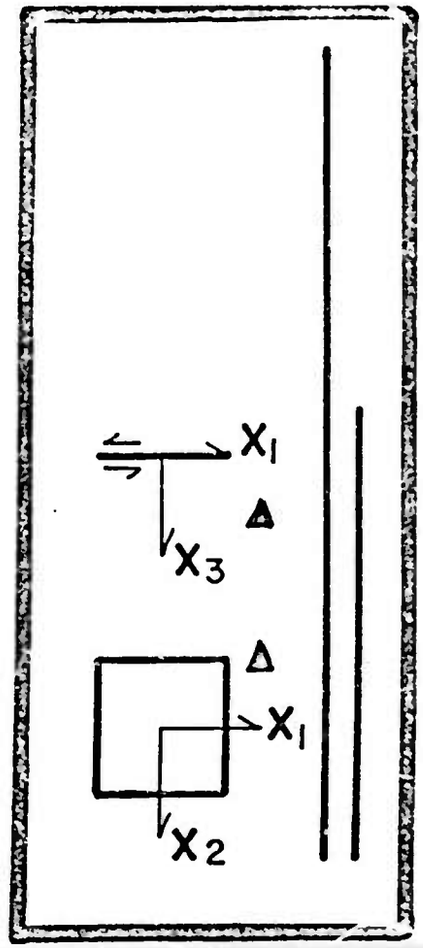

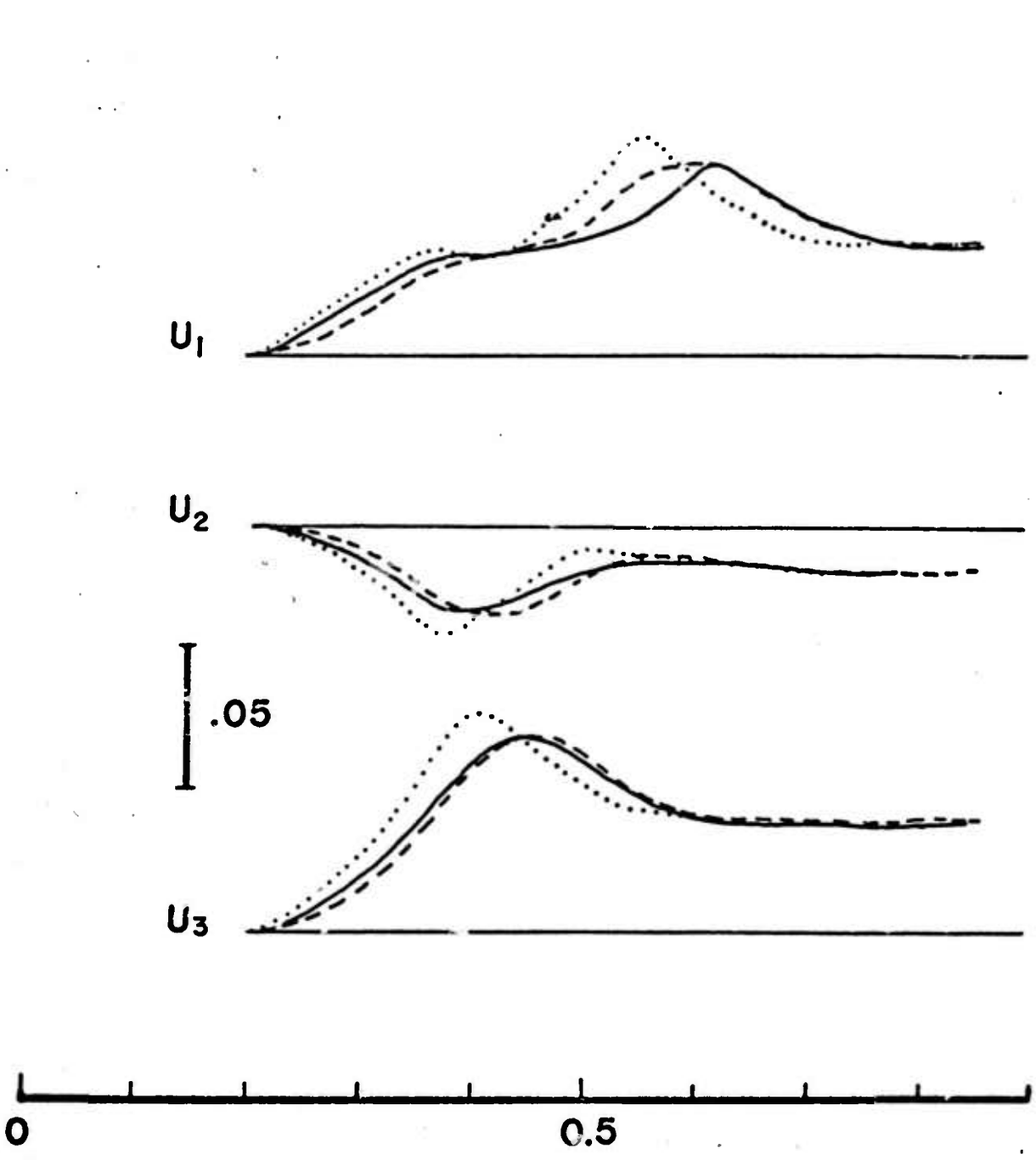

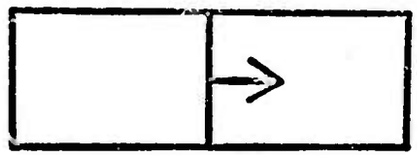

	V	τ
- - -	3.0	0.12
·····	3.0	0.0455
——	2.5	0.0455

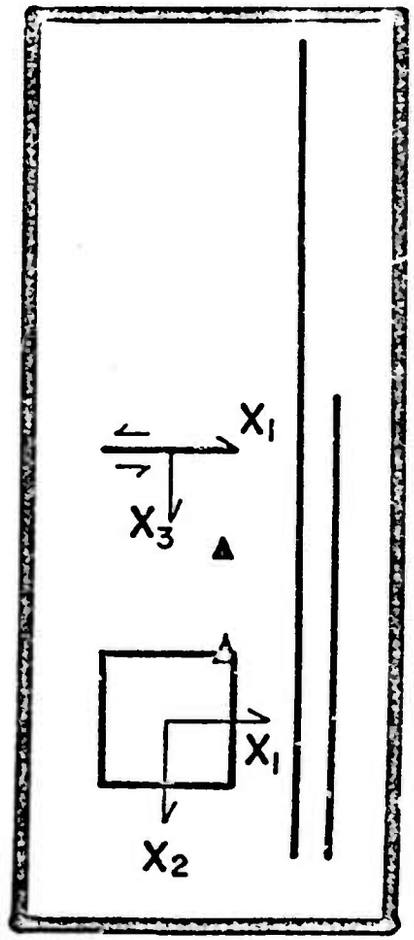

3c

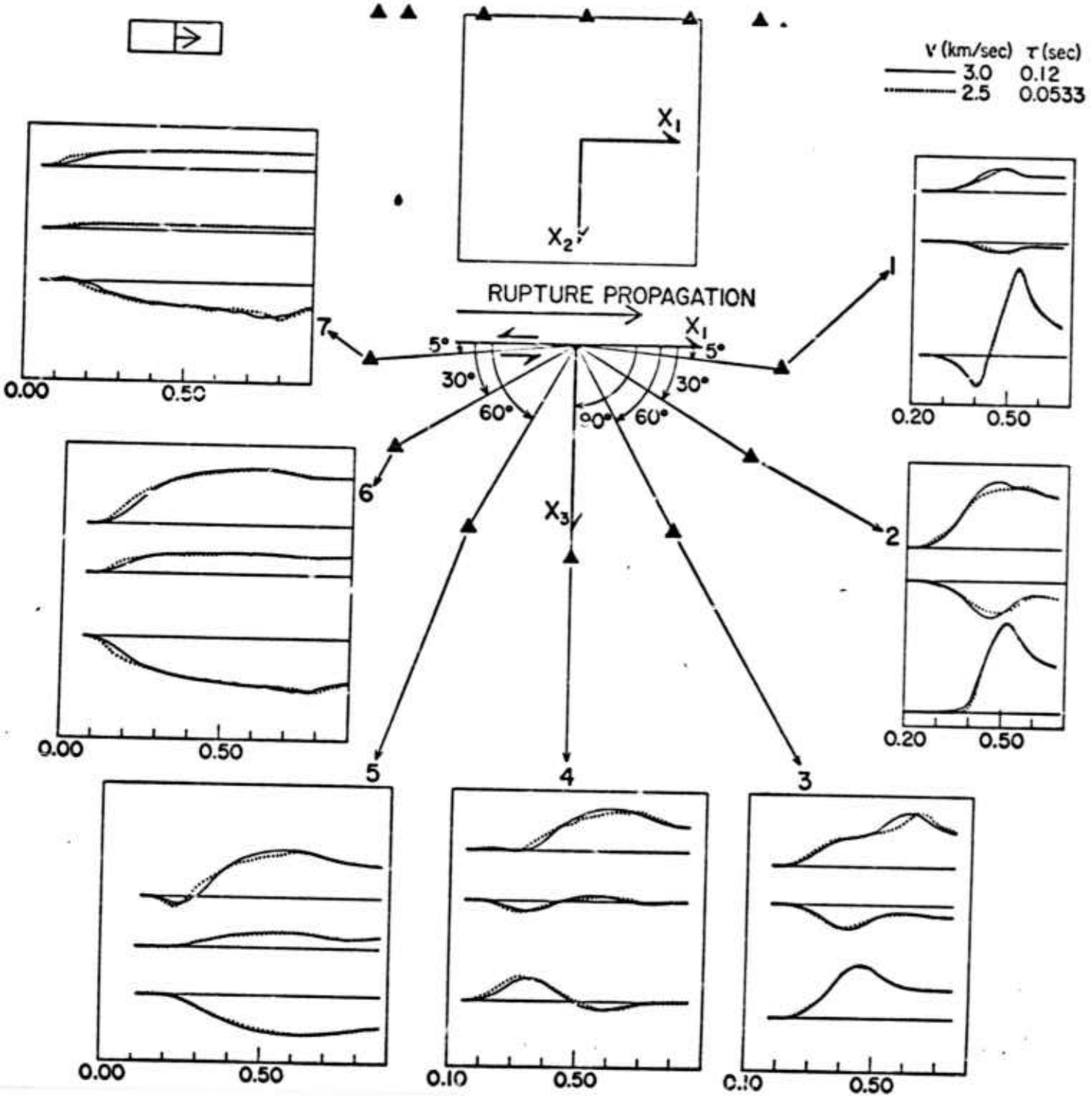
V (km/sec) τ (sec)
3.0 0.12
2.5 0.0533
X1
X2
X3
RUPTURE PROPAGATION
5°
5°
30°
30°
60°
60°
0°
1
2
3
4
5
6
7
0.00
0.50
0.20
0.50
0.00
0.50
0.20
0.50
0.00
0.50
0.10
0.50
0.10
0.50

3d

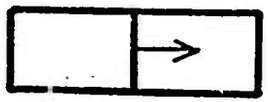

V	τ	
3.0	0.12	——
2.5	0.0533	.....

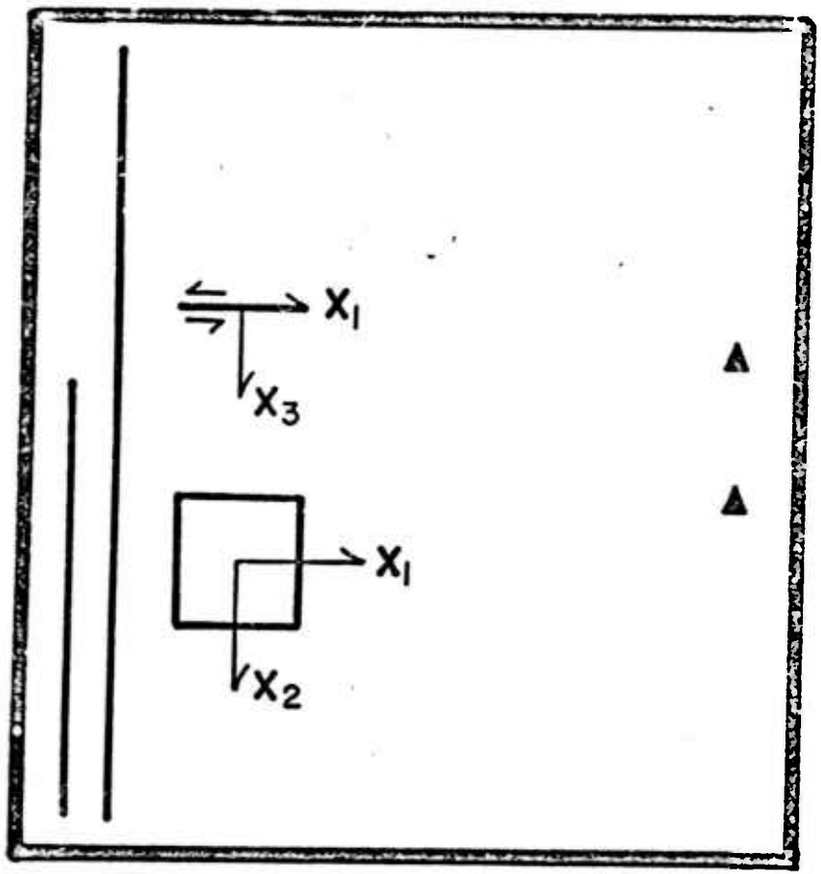

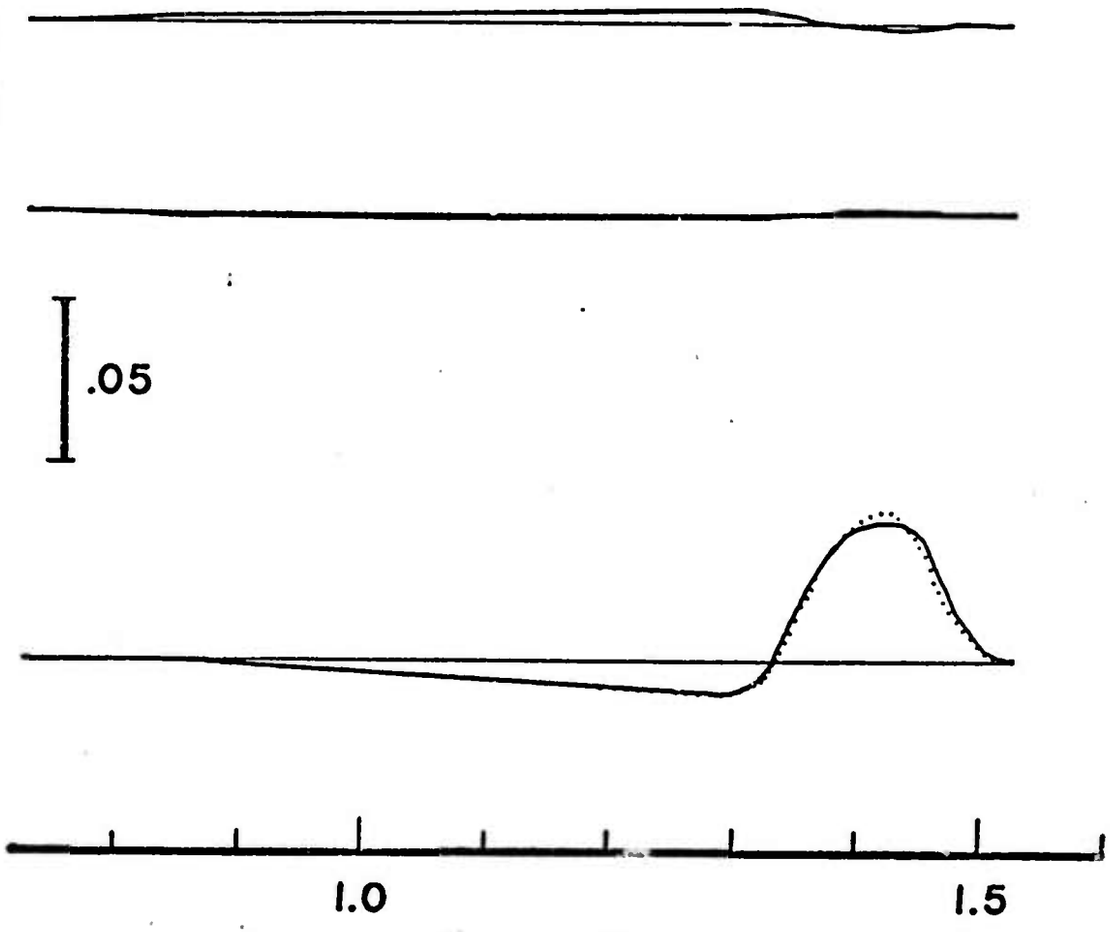

se

V	τ	
3.3	0.2	—
2.8	0.0647	.....

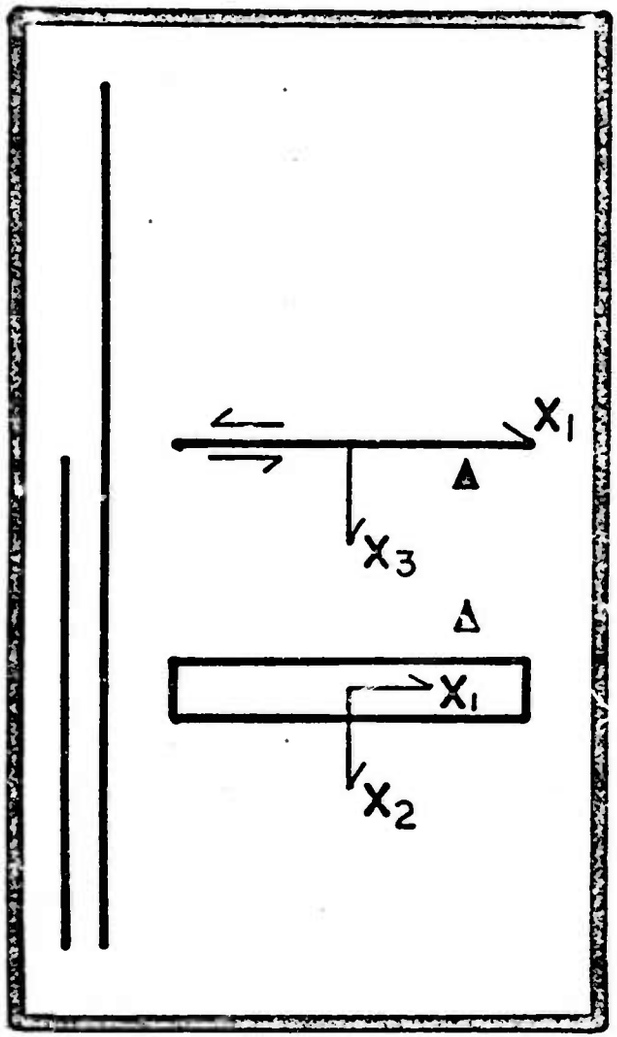

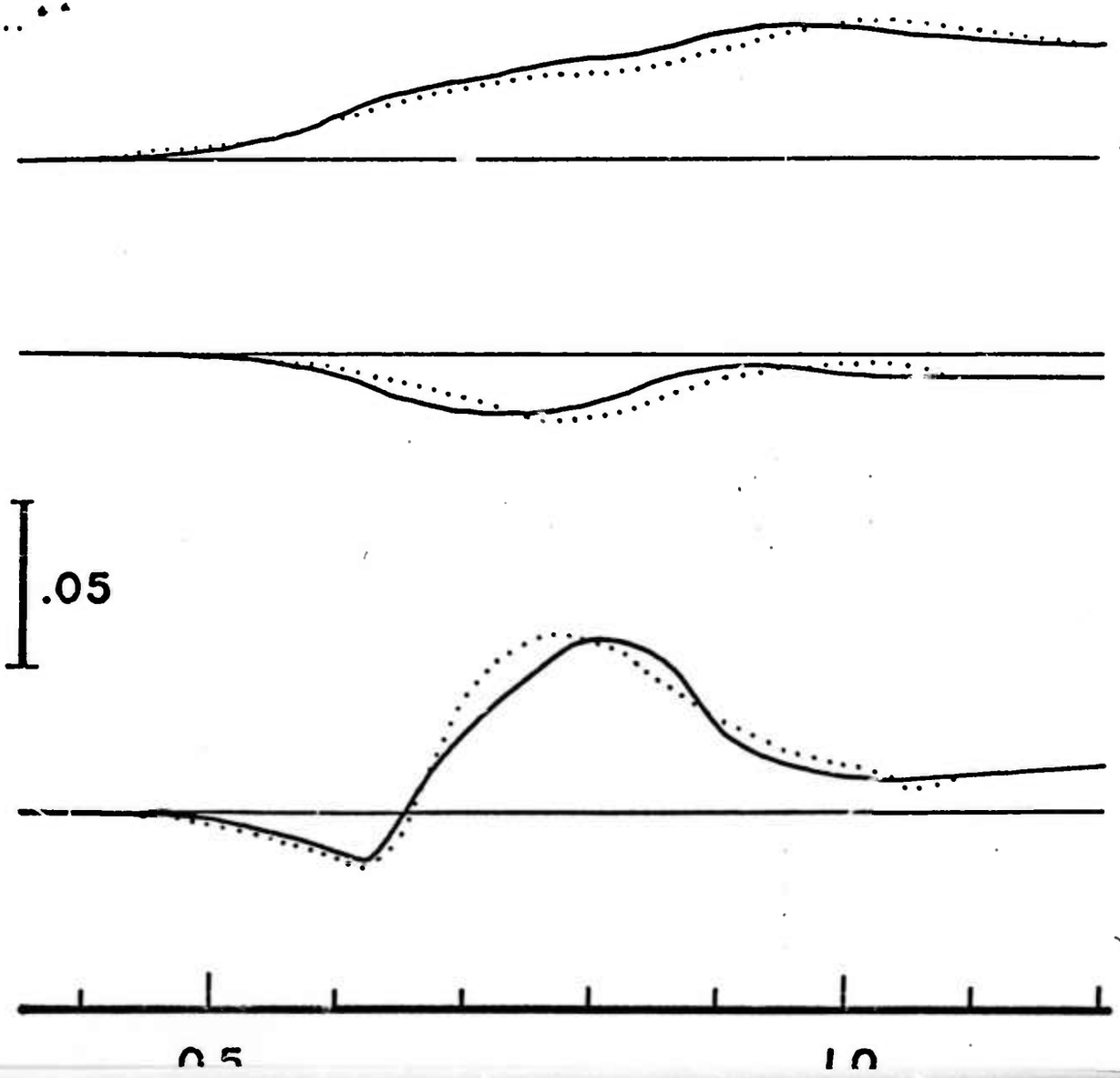

65

4a

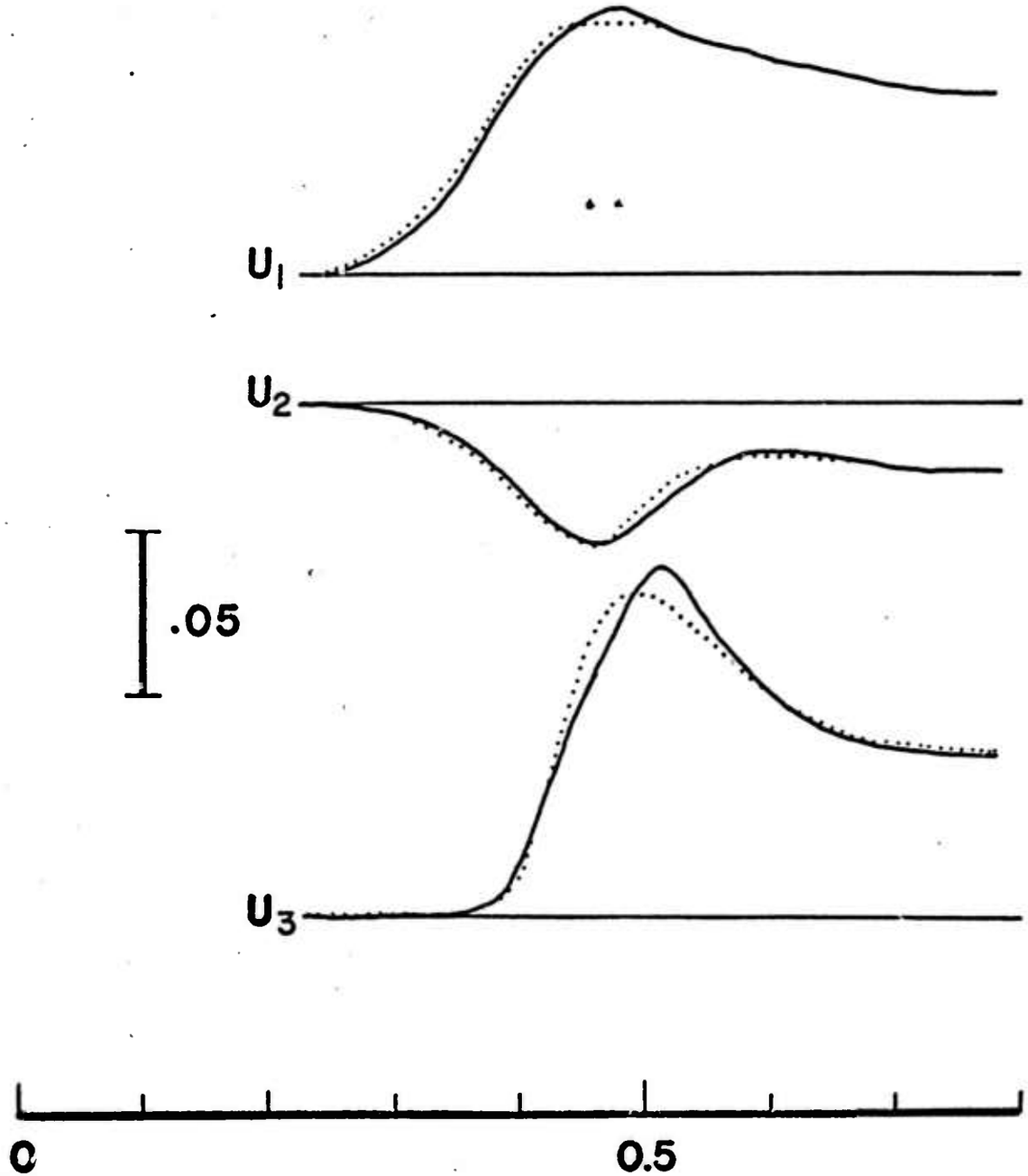

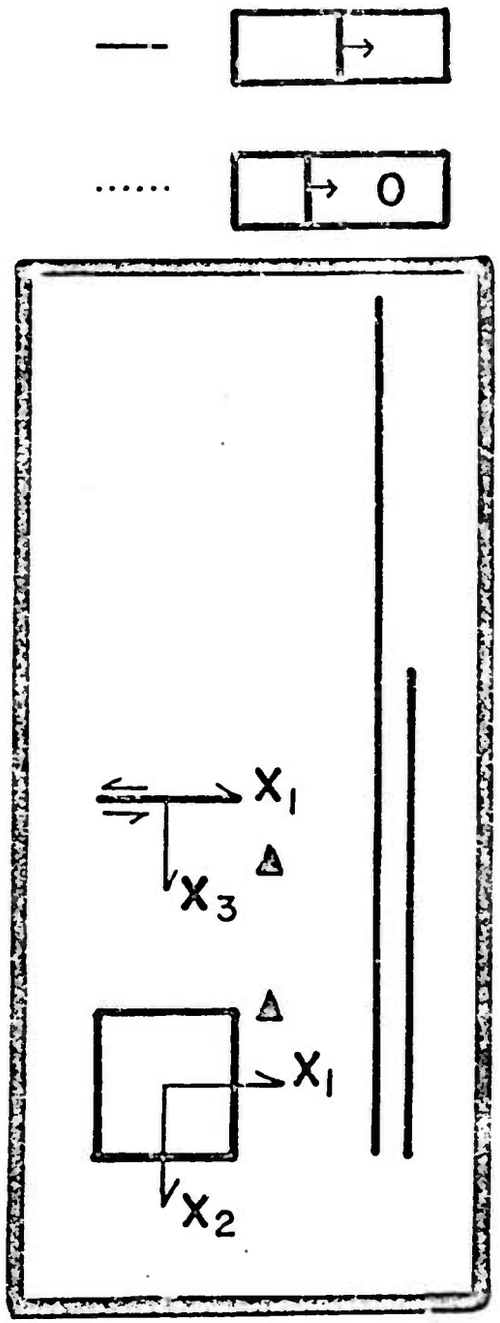

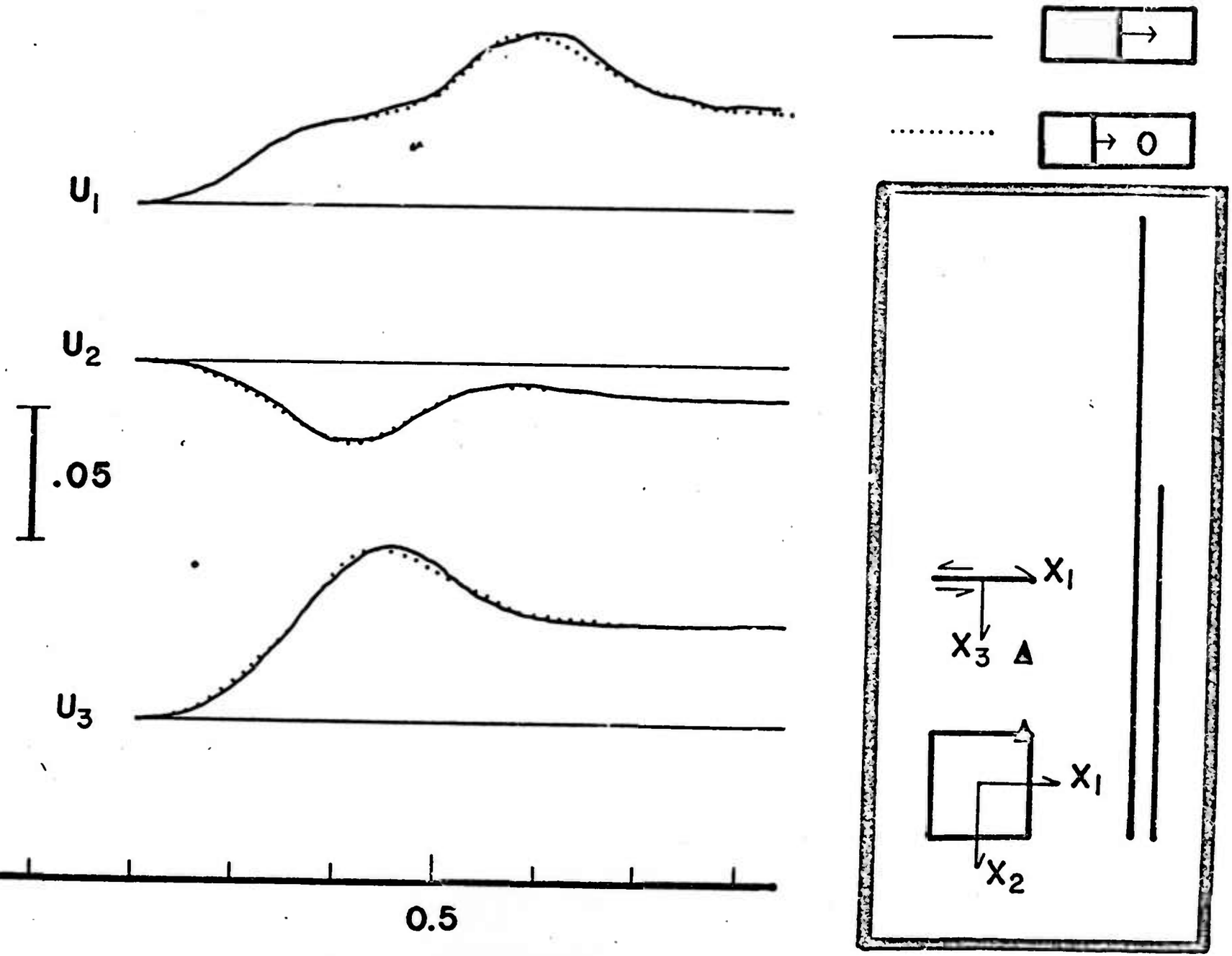
U1
U2
U3
.05
0
0.5
X1
X3
Δ
X1
X2

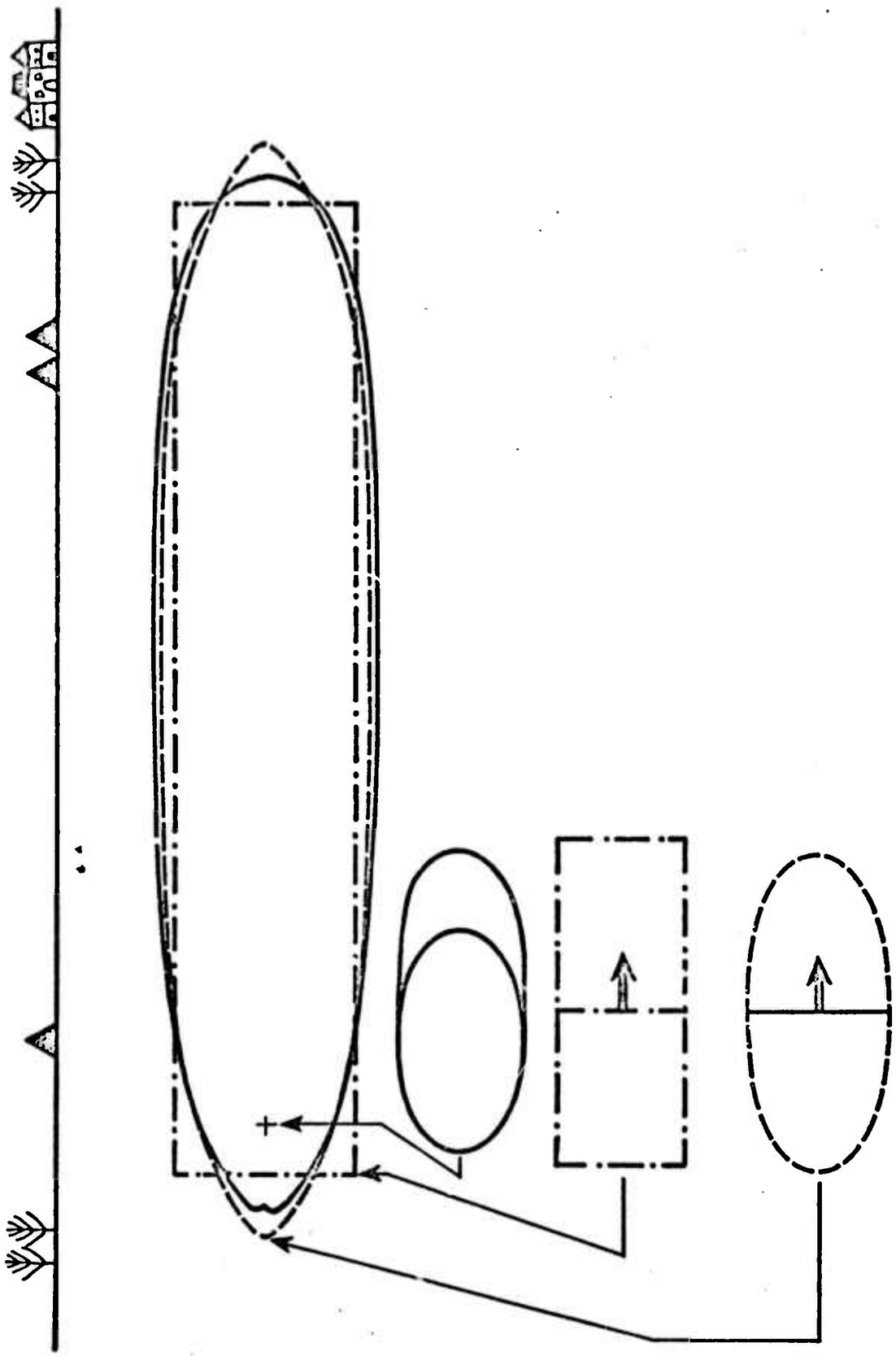

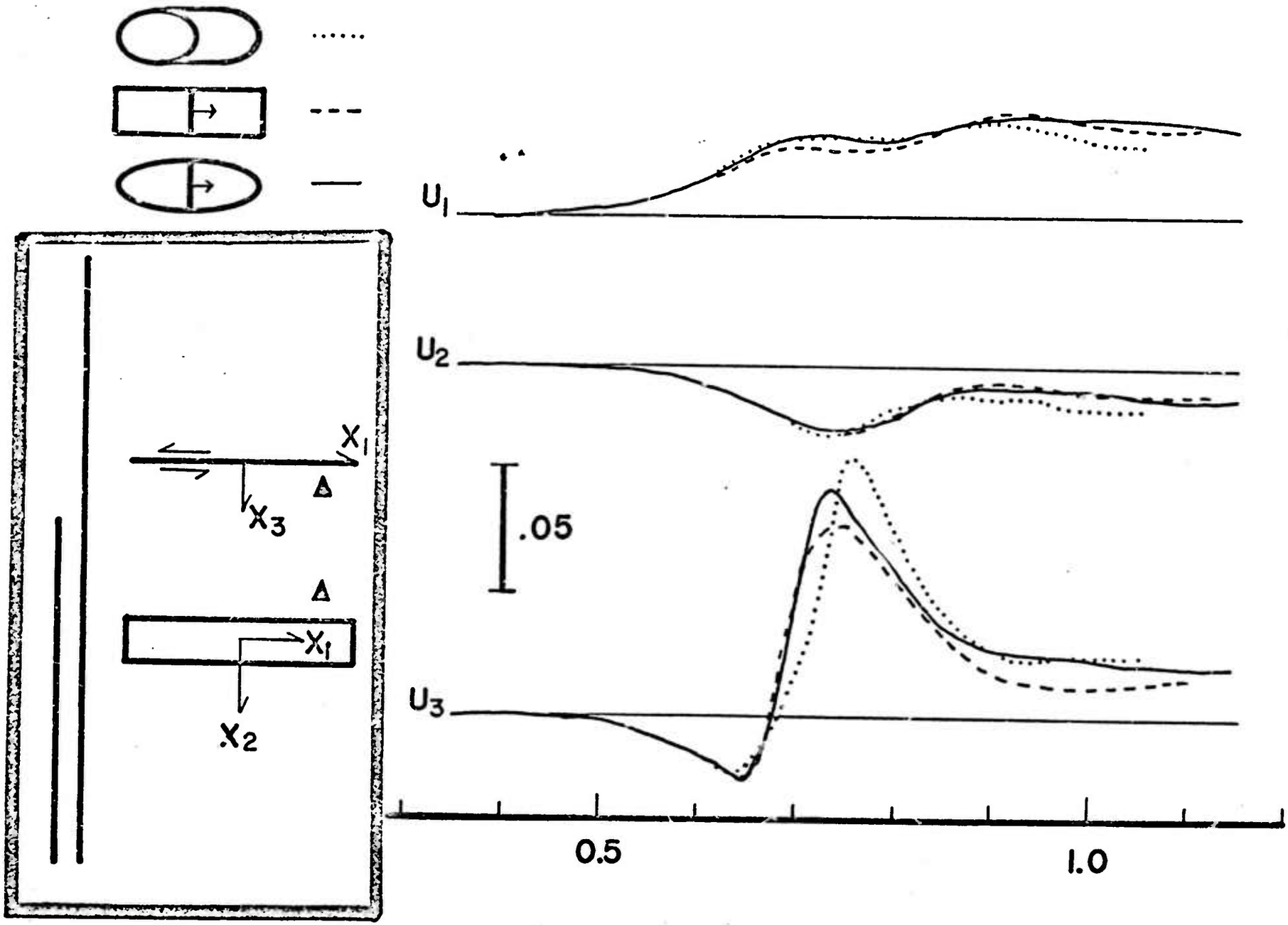
U1
U2
U3
.05
X1
X3
X1
X2
0.5
1.0

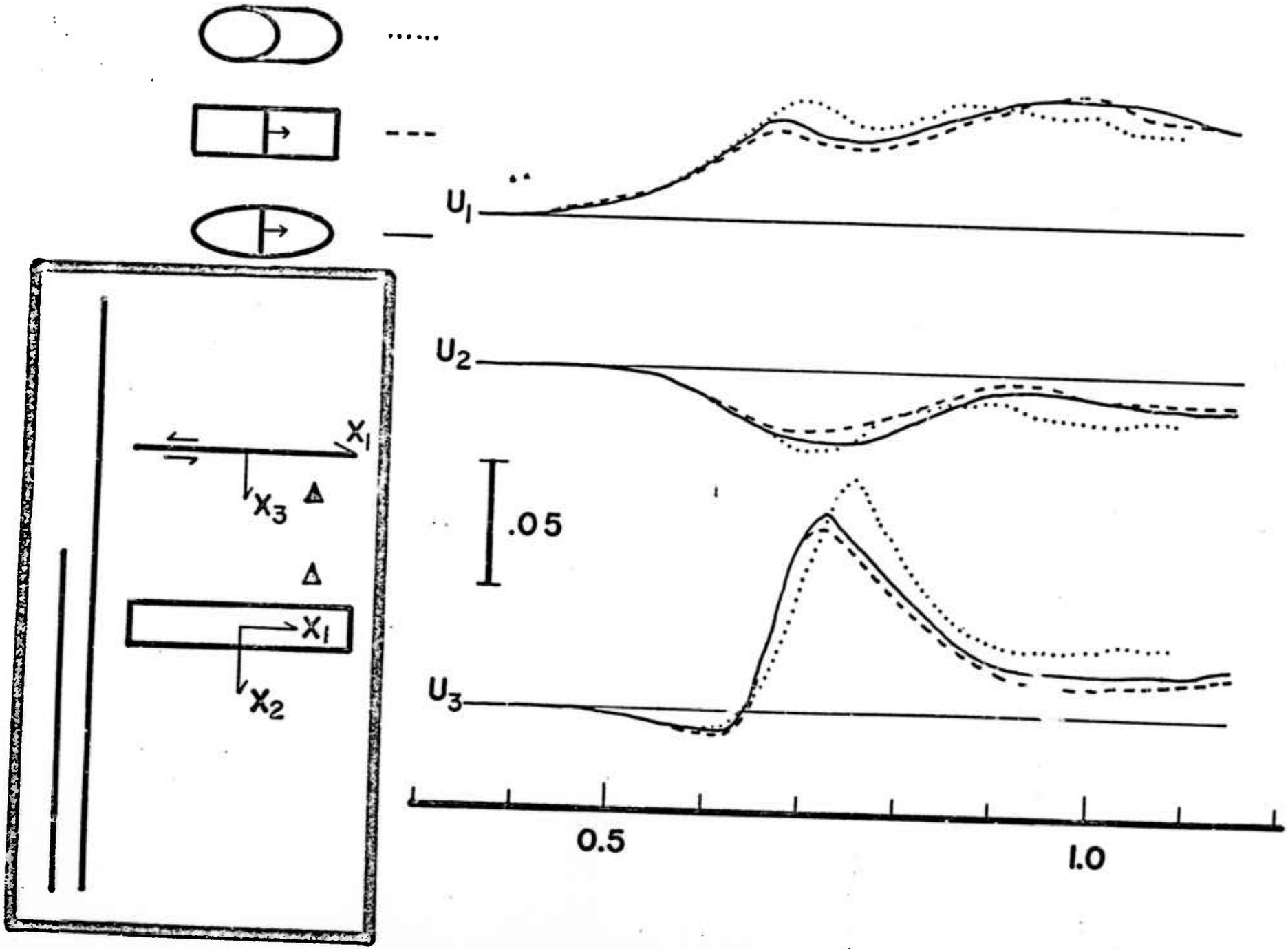
U1
U2
U3
.05
X1
X3
X1
X2
0.5
1.0

bc

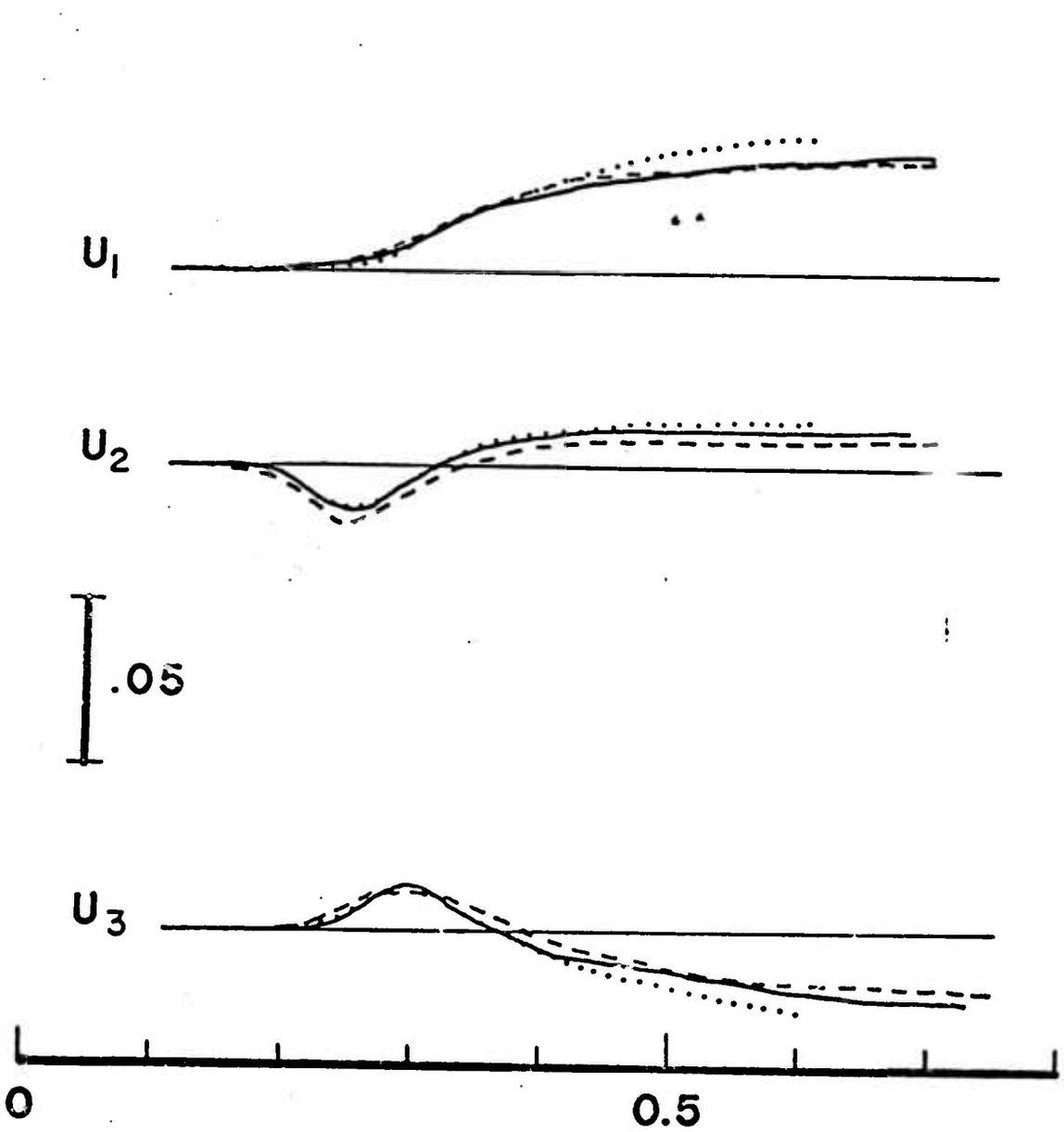

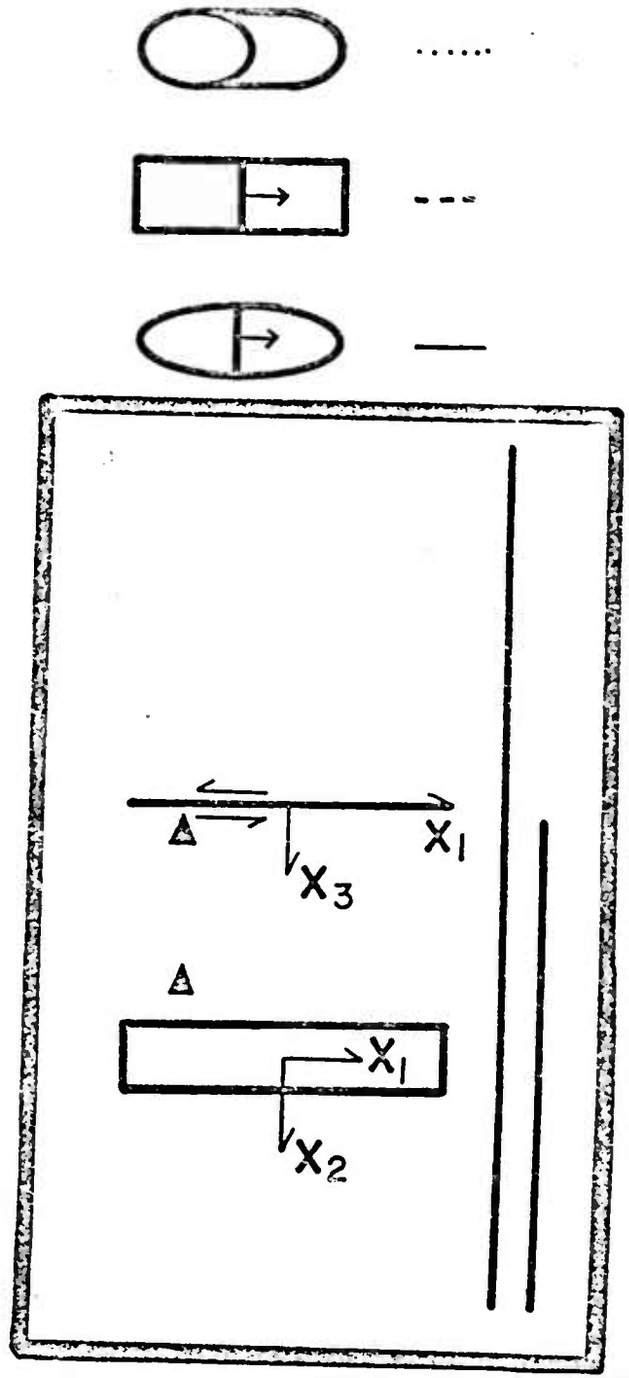

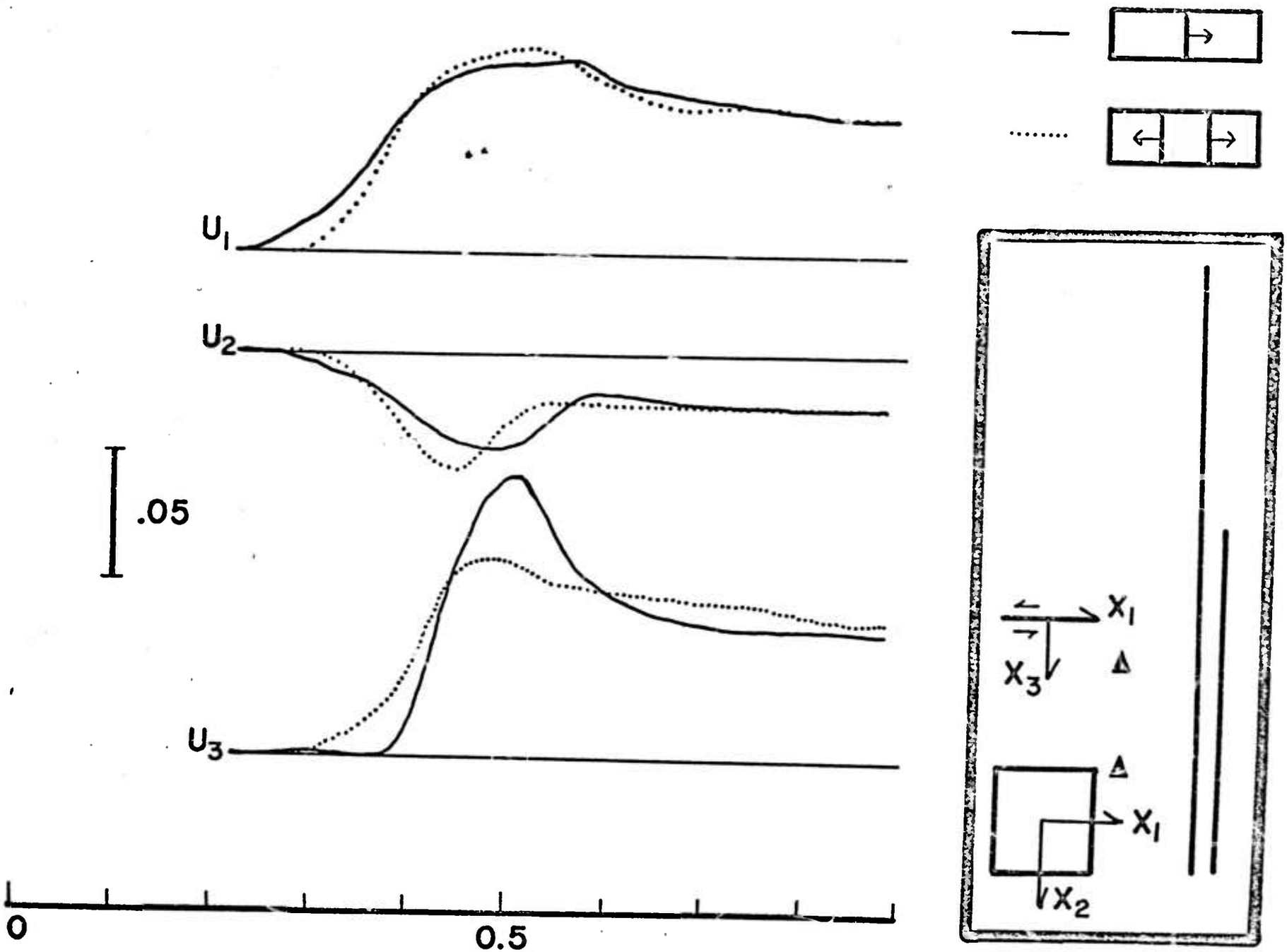
U1
U2
U3
.05
0
0.5
X1
X3
Δ
Δ
X1
X2

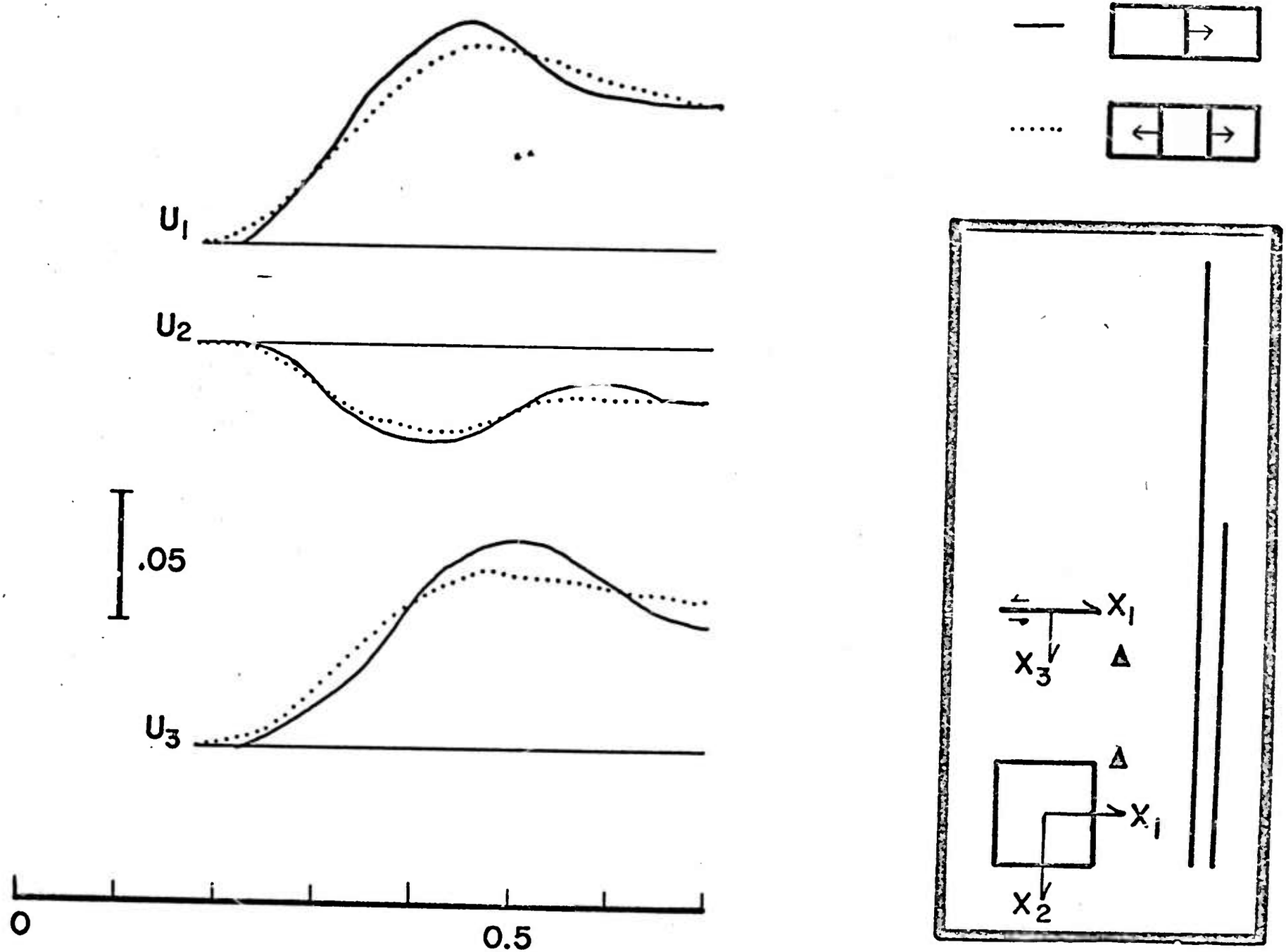
U1
U2
U3
.05
0
0.5
X1
X3
Δ
Δ
X1
X2

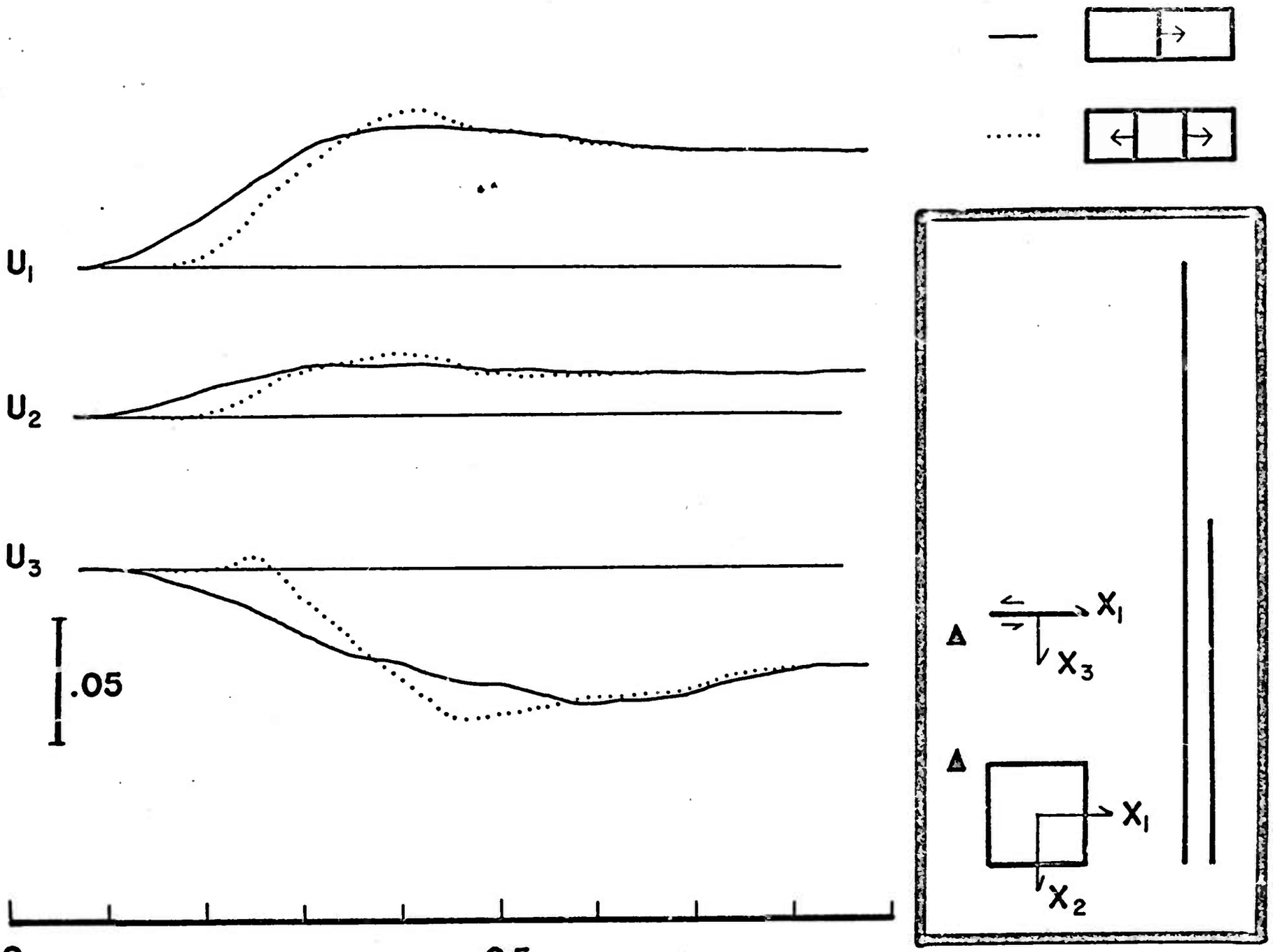
U1
U2
U3
.05
0
0.5
X1
X3
X1
X2

6c

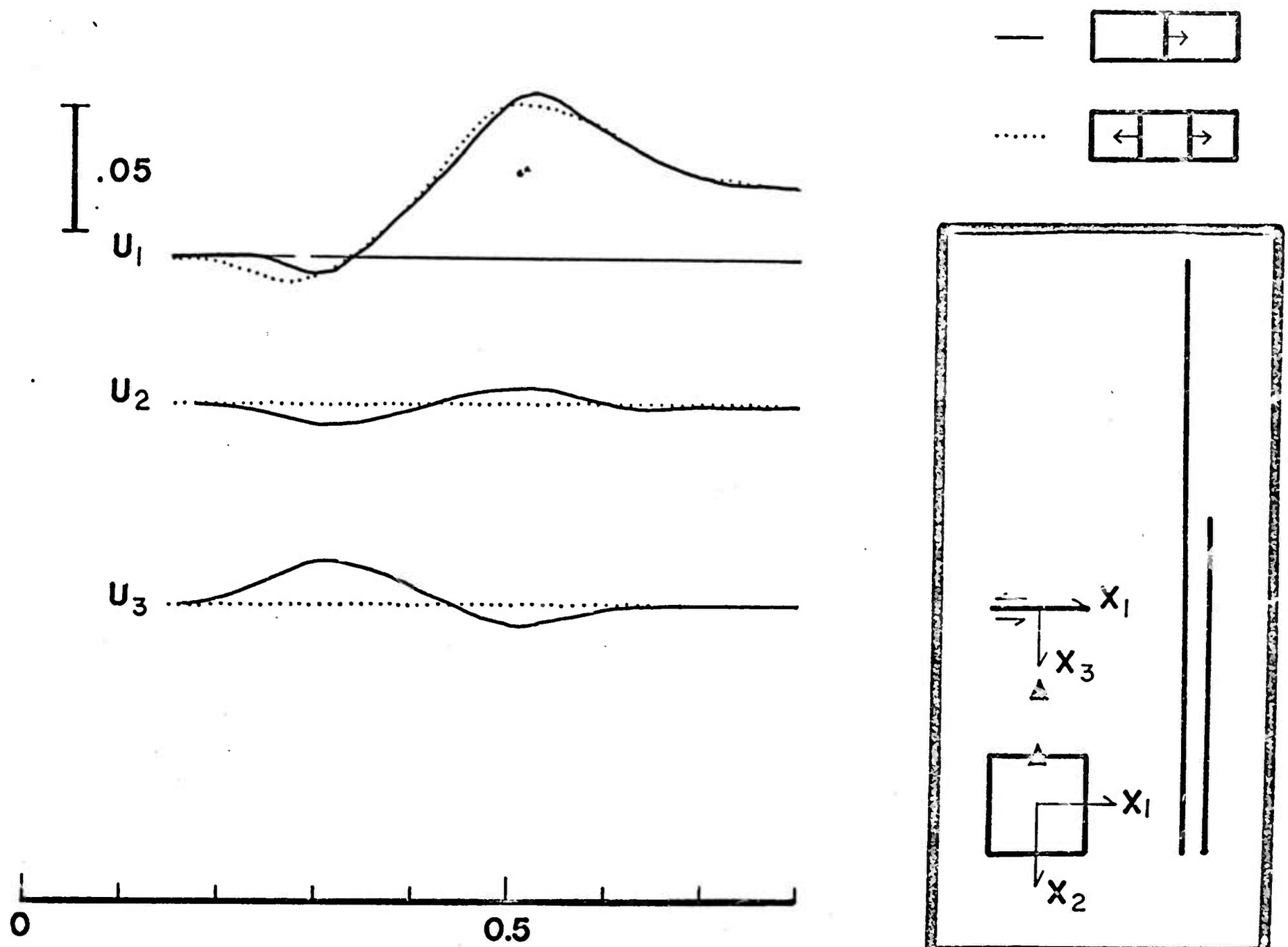

9a

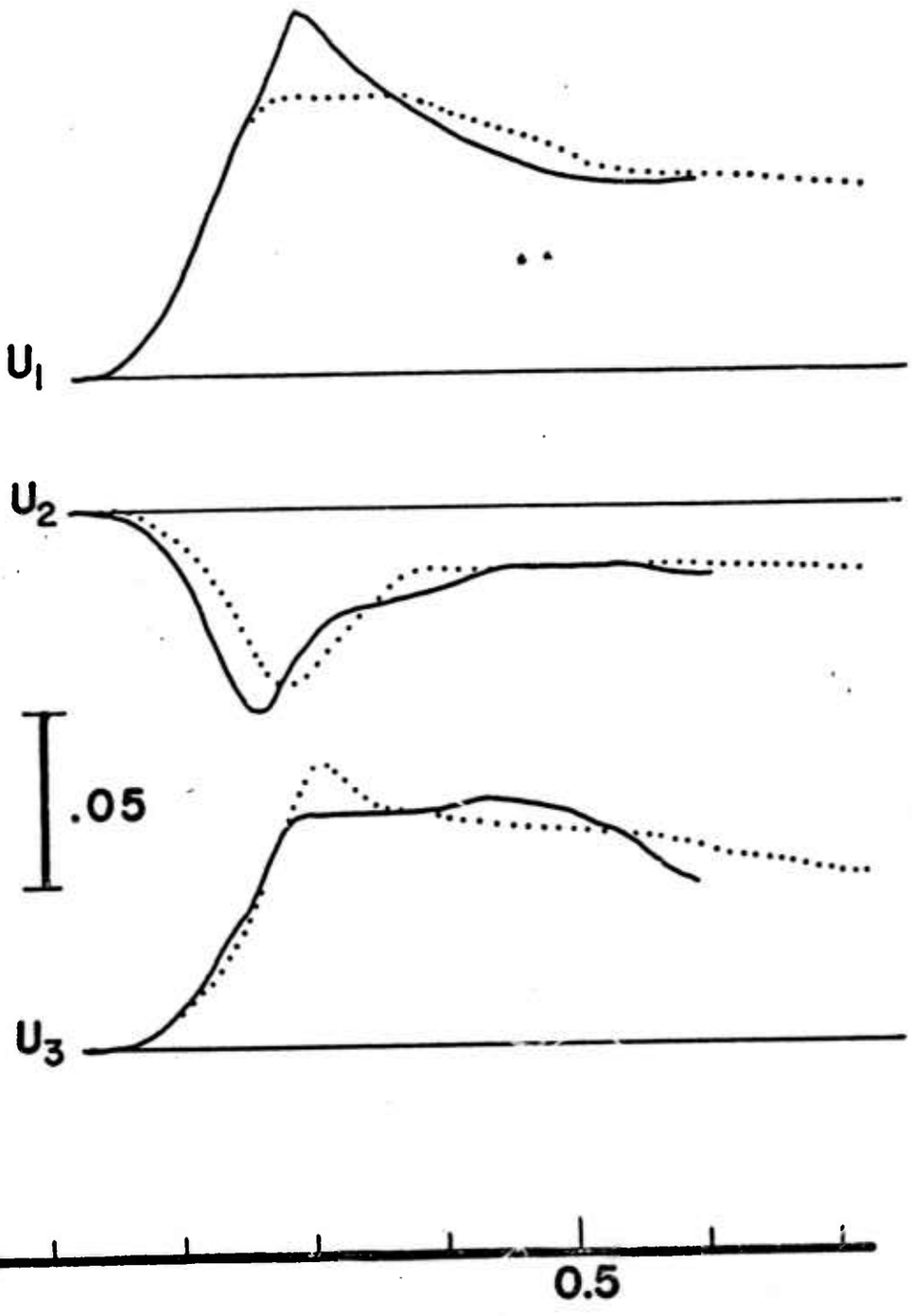

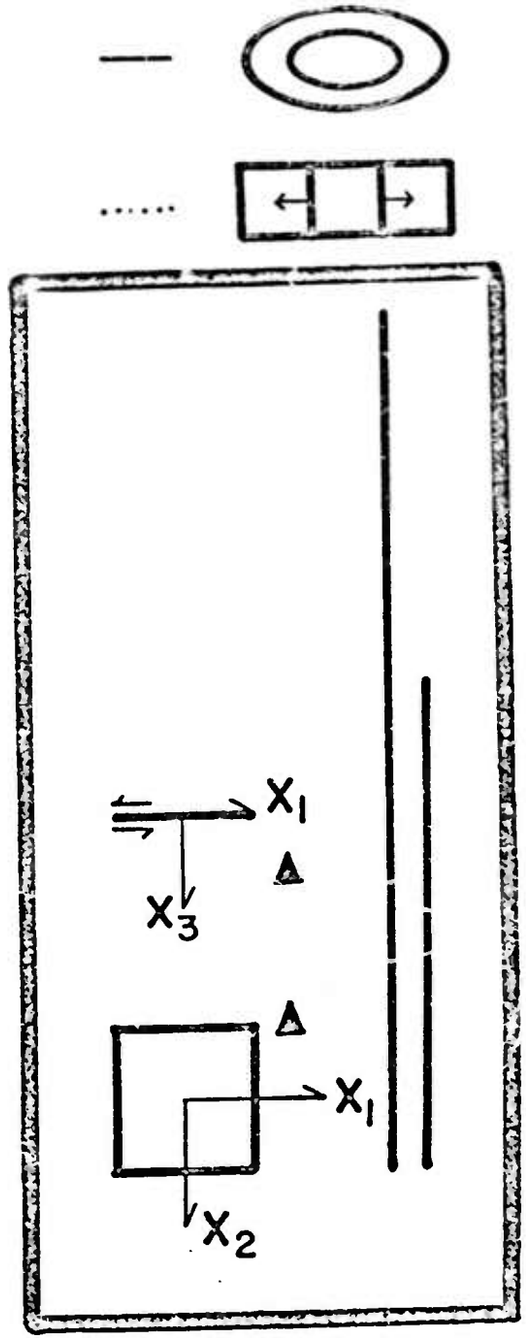

7a

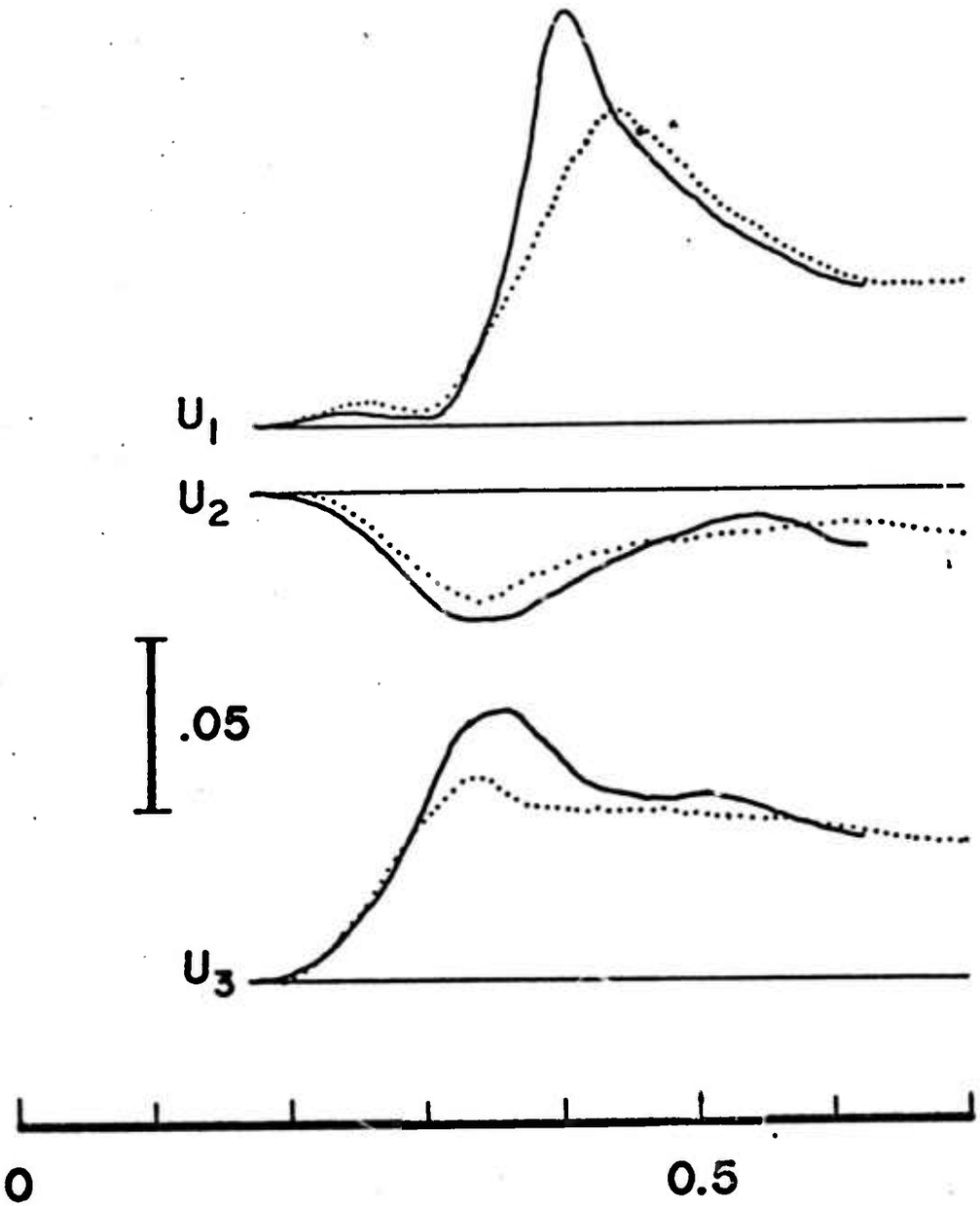
U1
U2
.05
U3
0
0.5

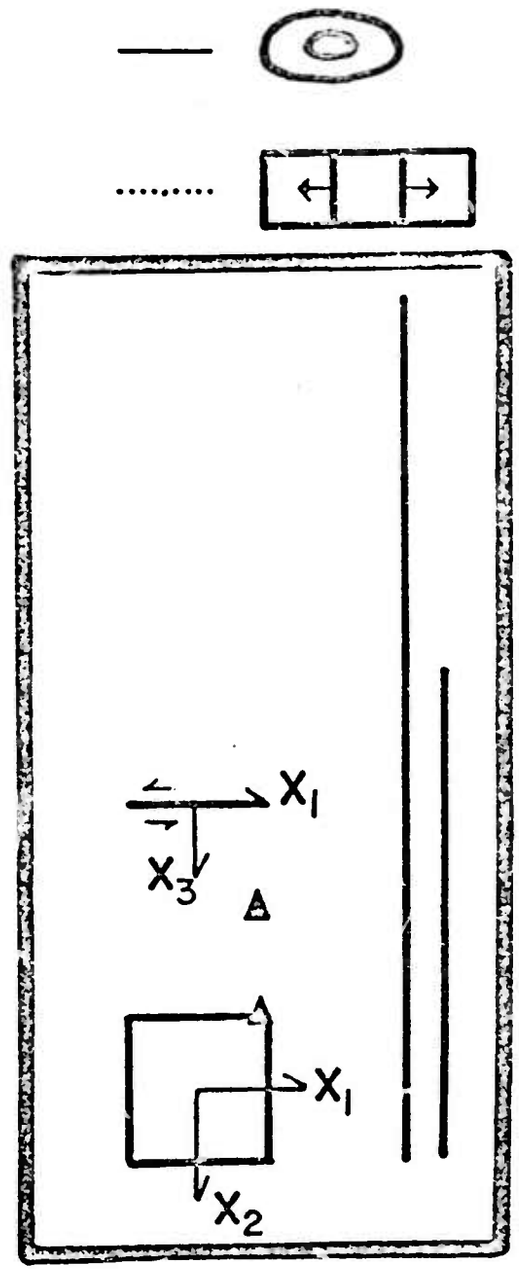
X1
X3
A
X1
X2

1c

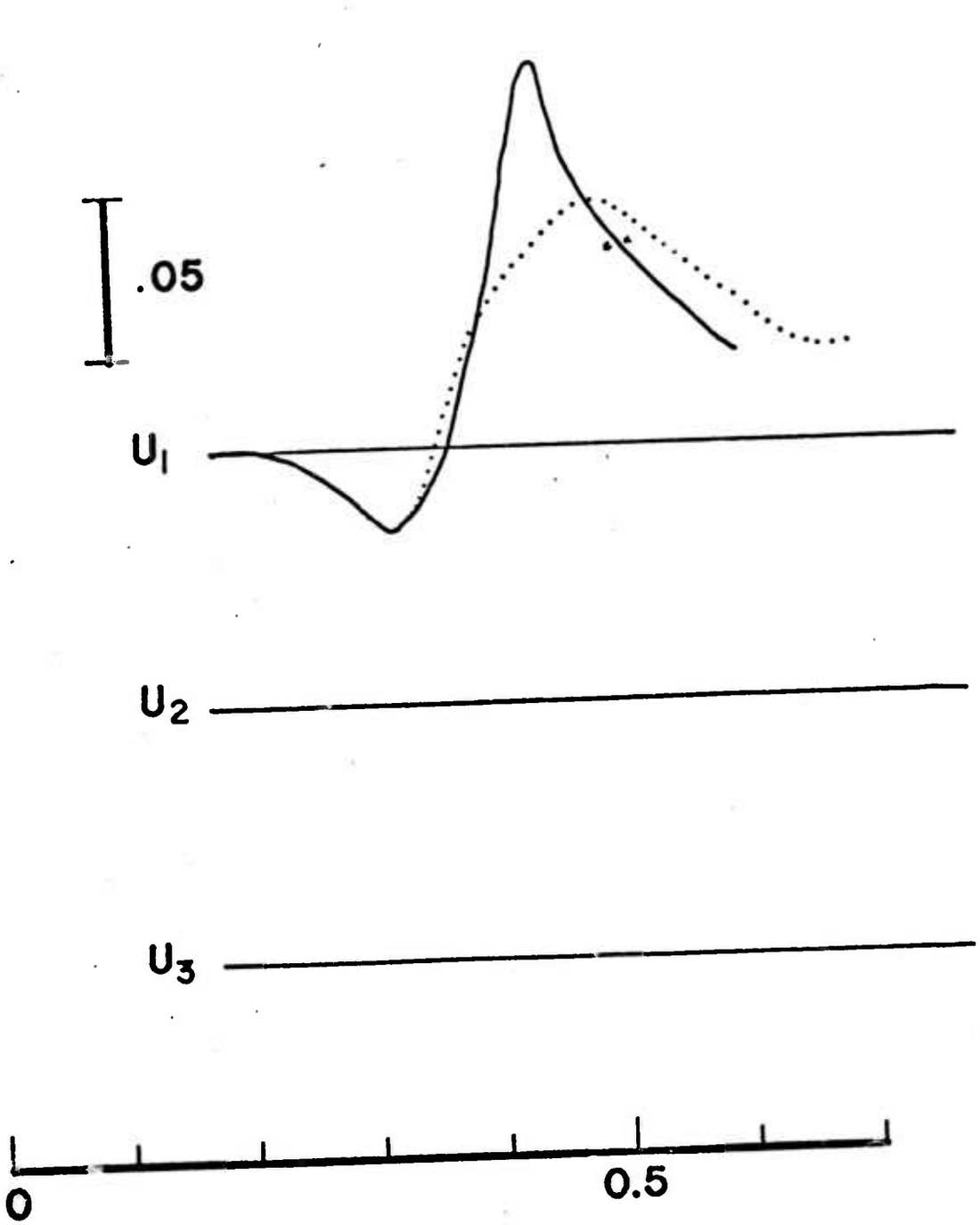

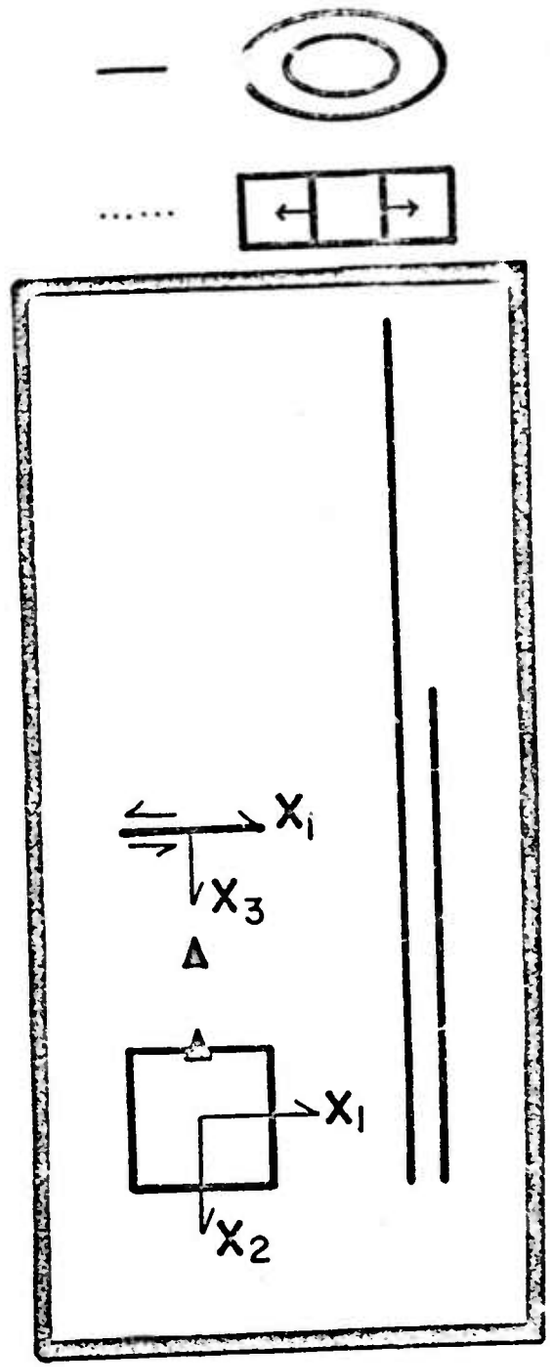

10c

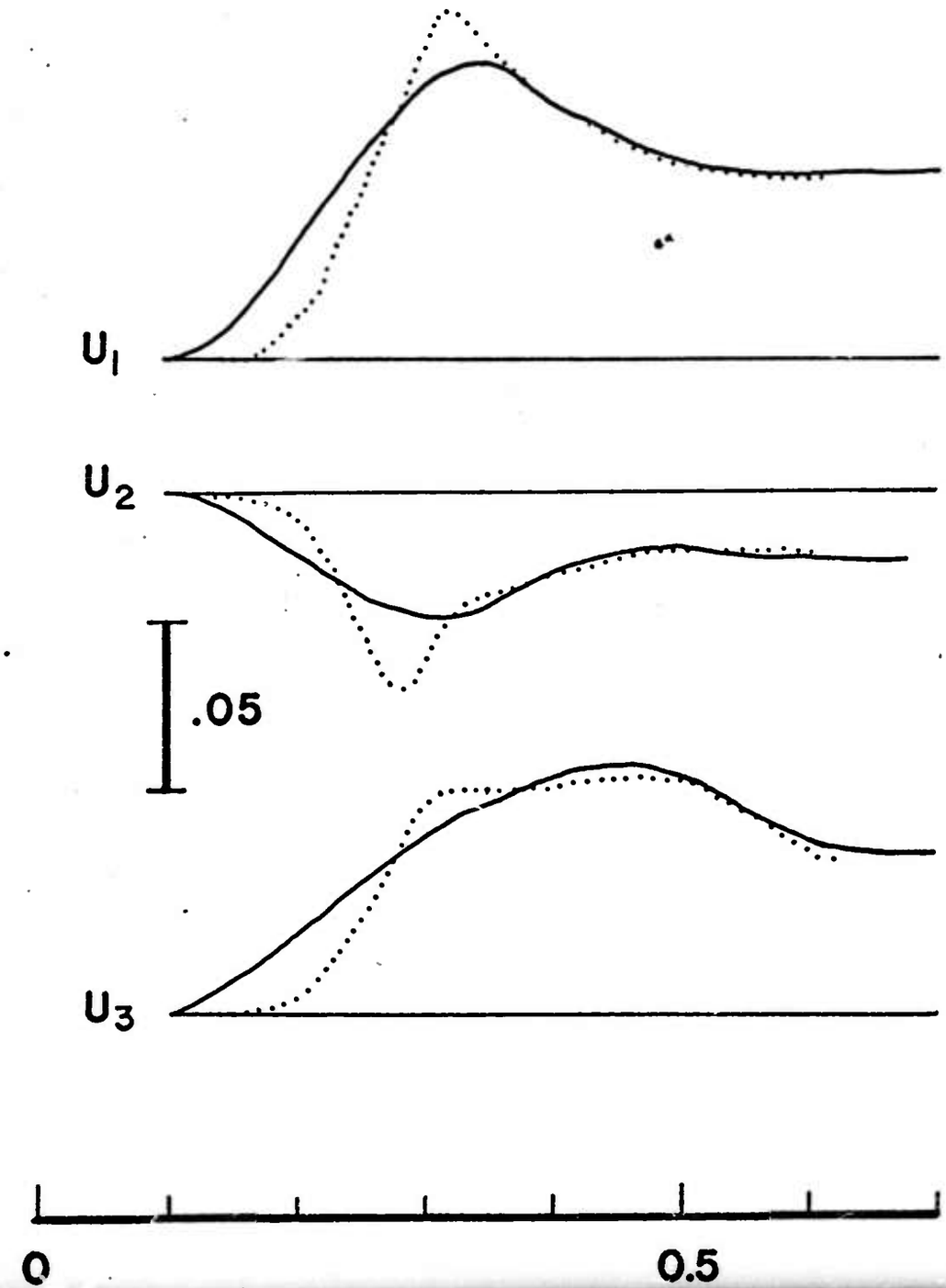

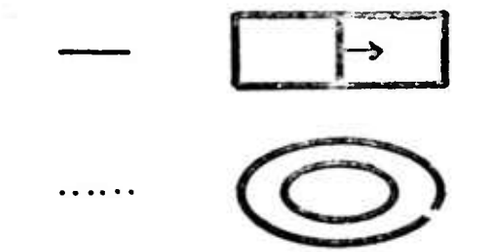

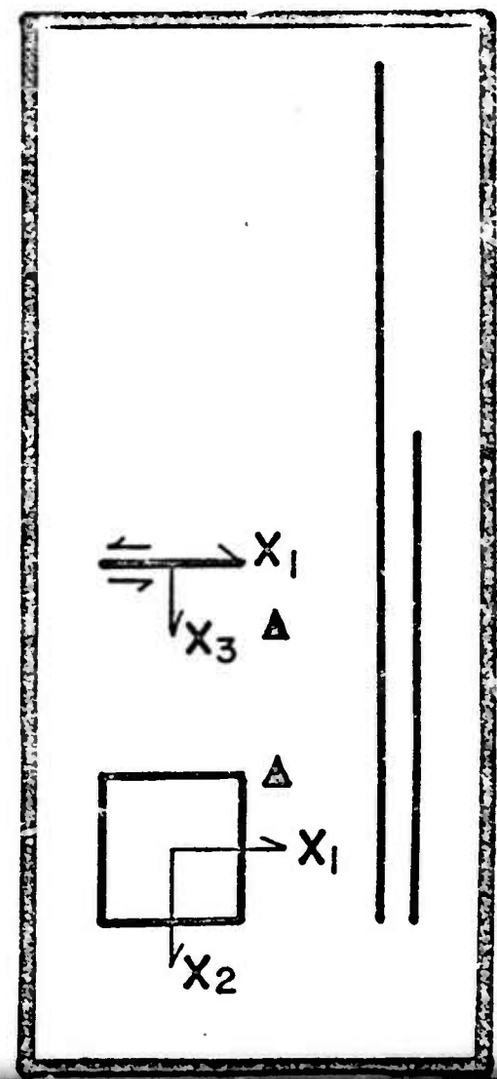

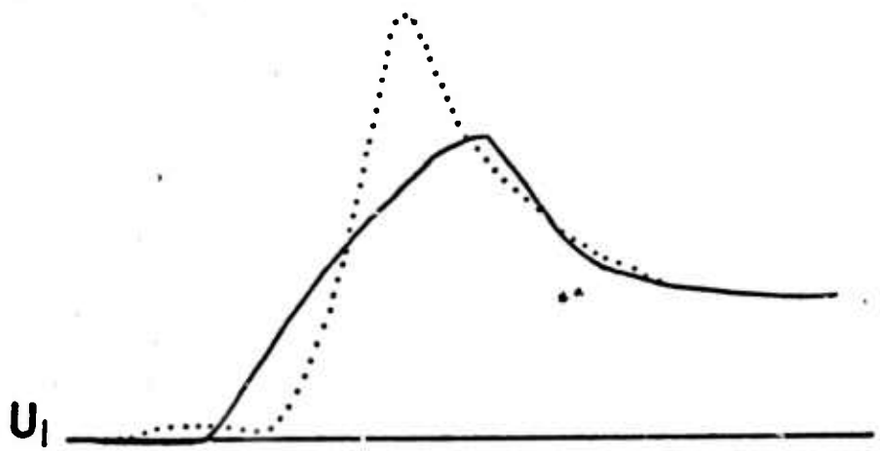
U1


U2


.05
U3


0
0.5

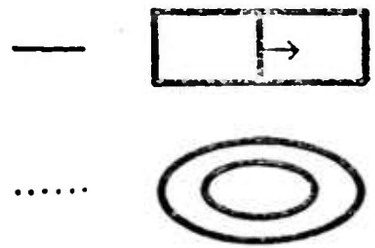

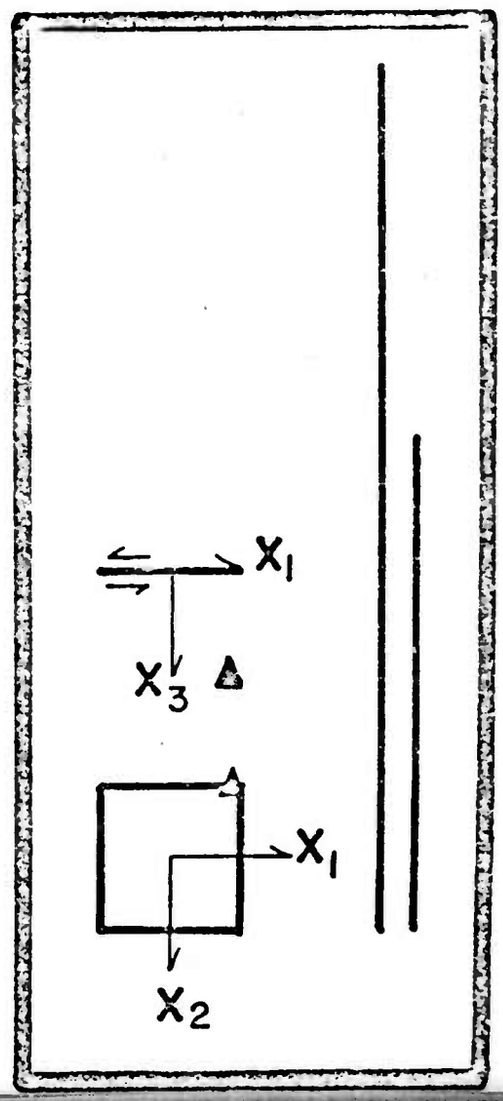
X1
X3
X1
X2

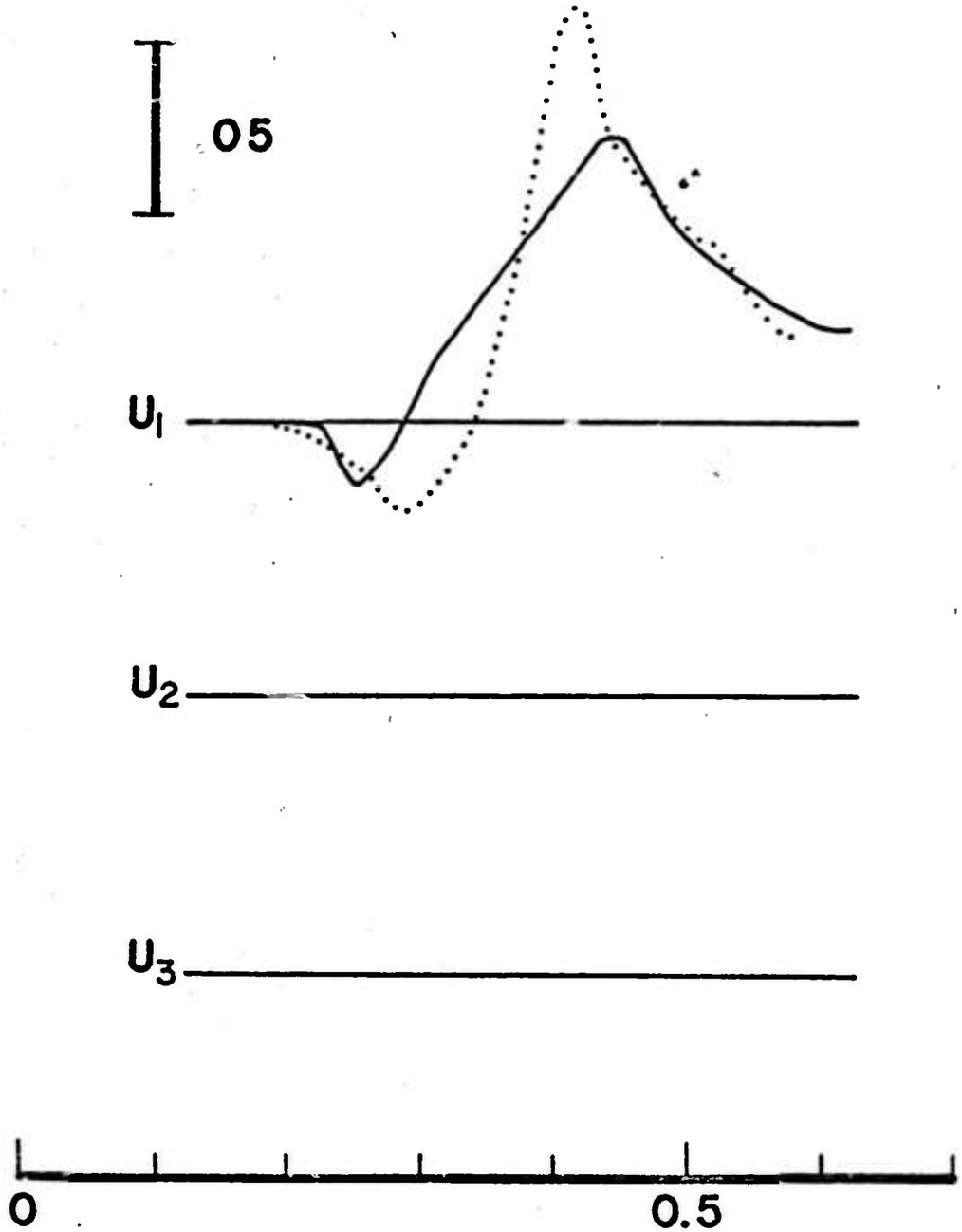
05
U1
U2
U3
0
0.5

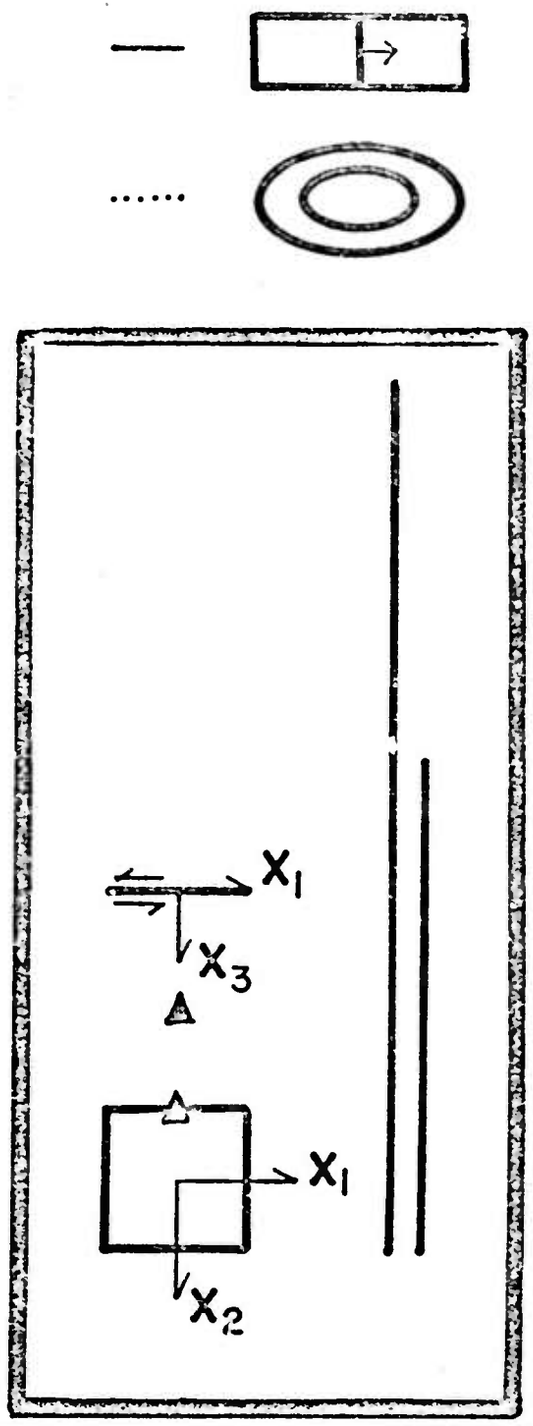
X1
X3
X1
X2

1a

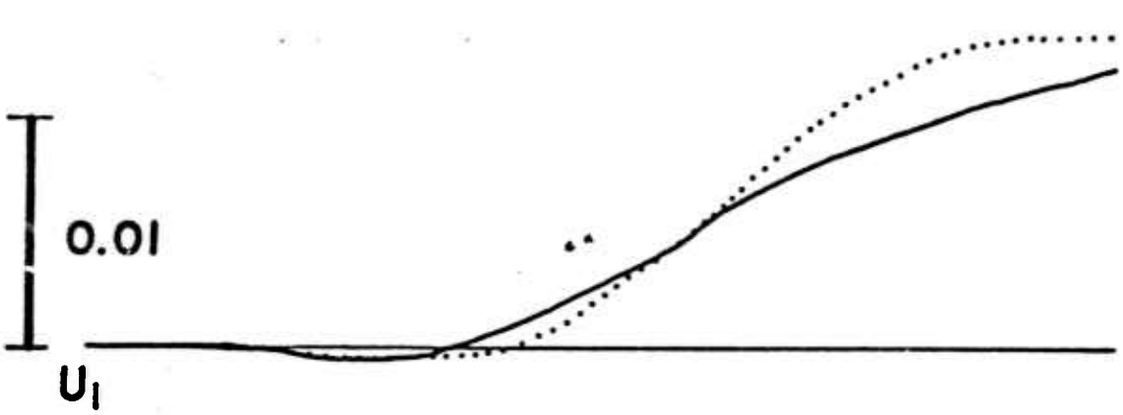

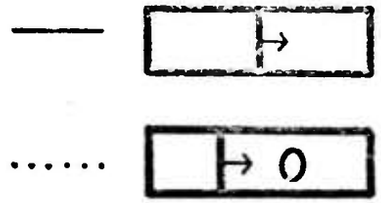

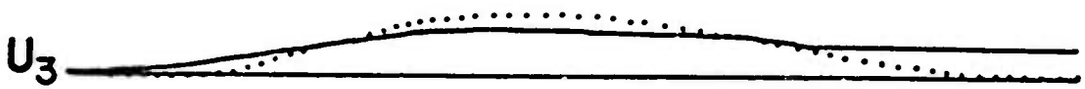

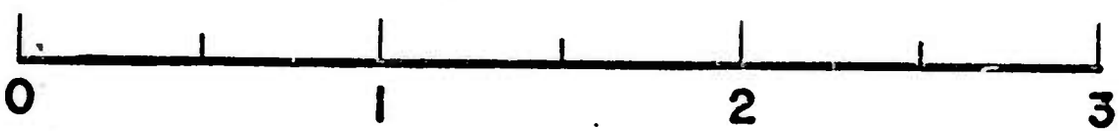

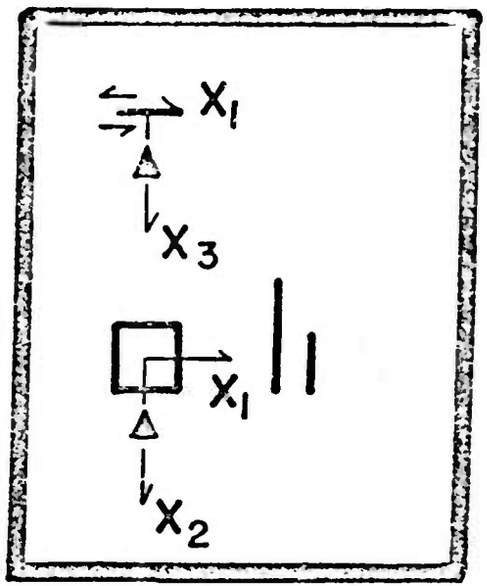

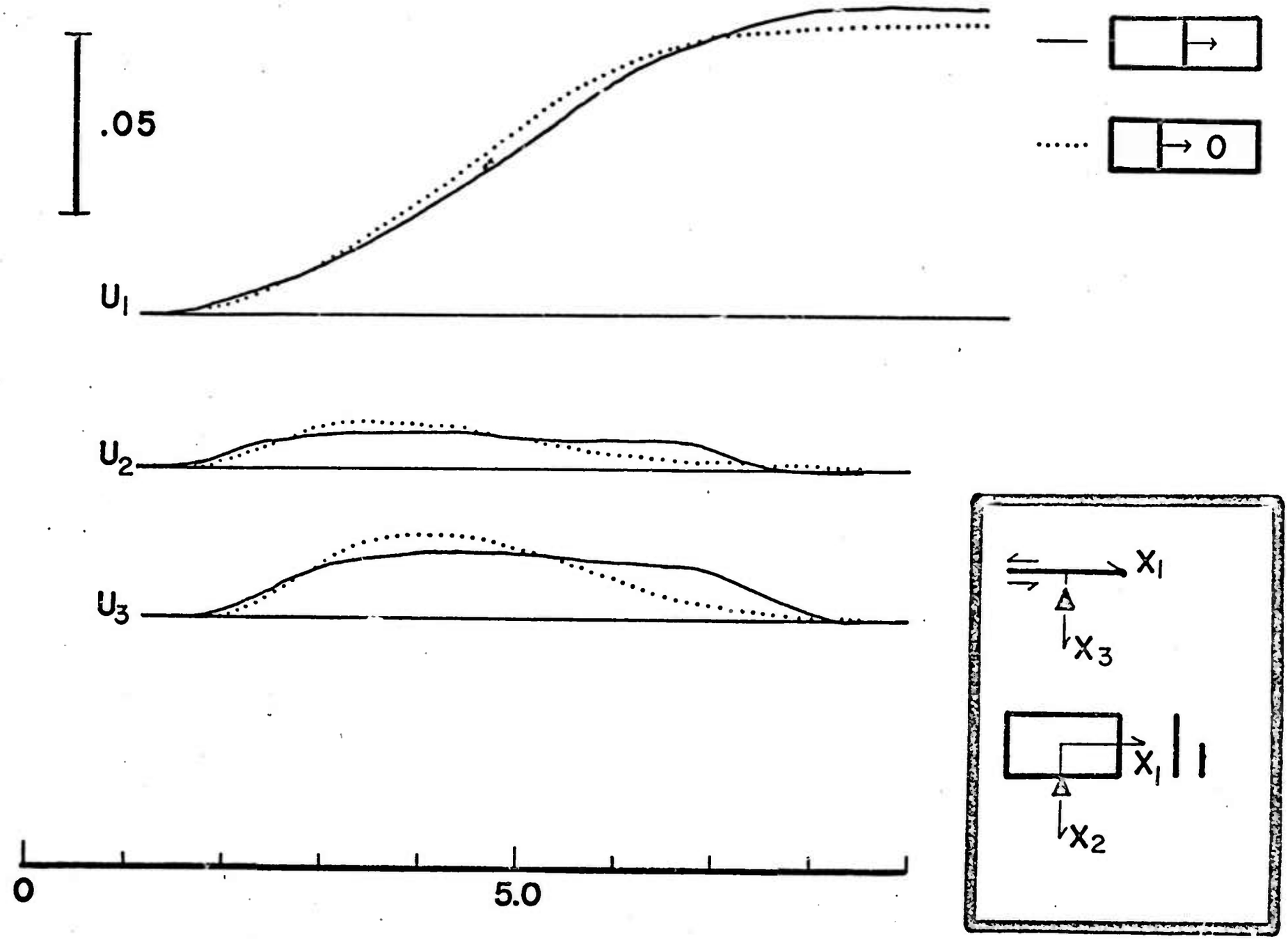
.05
U1
U2
U3
0
5.0
X1
X3
X1
X2

11c

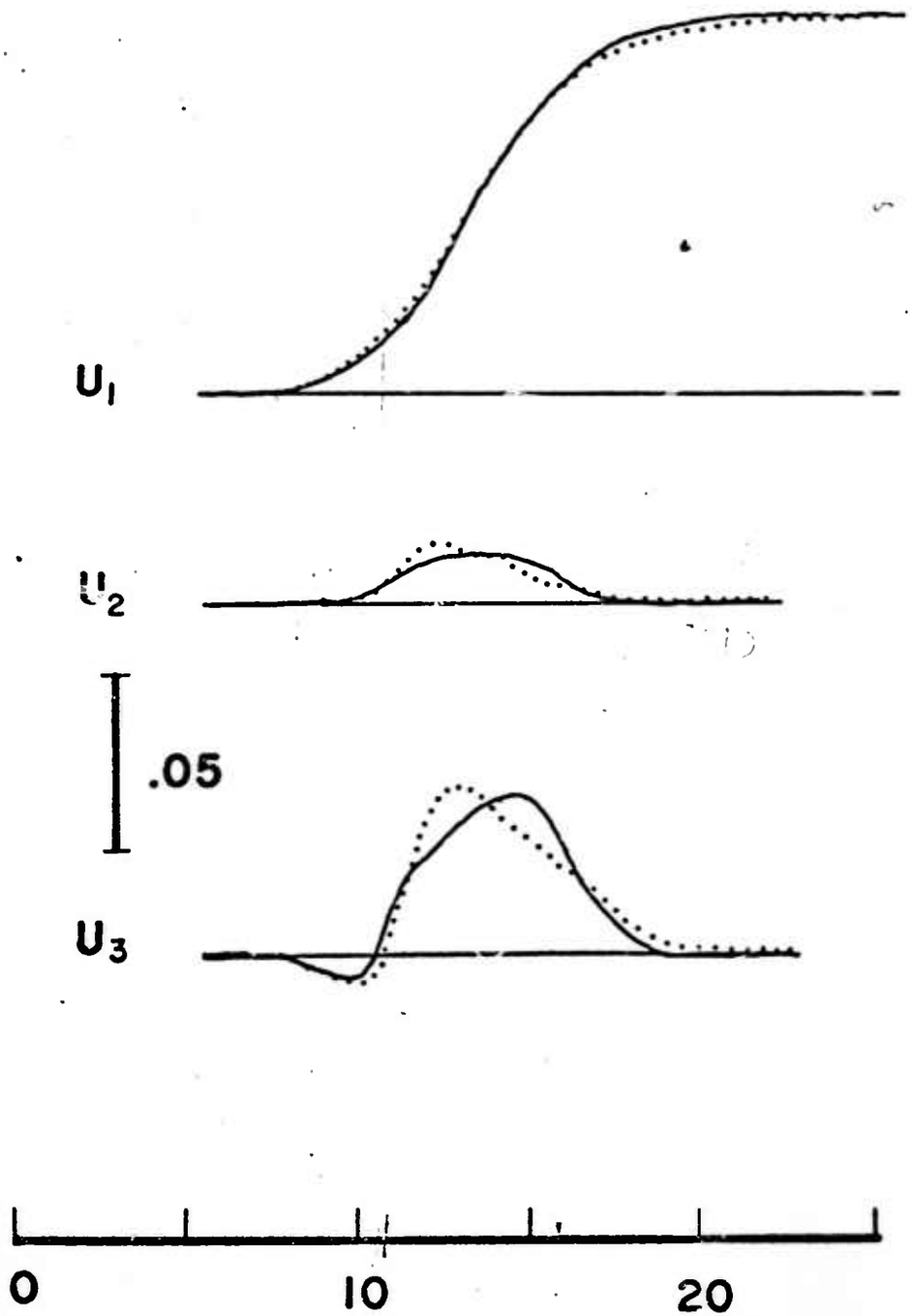

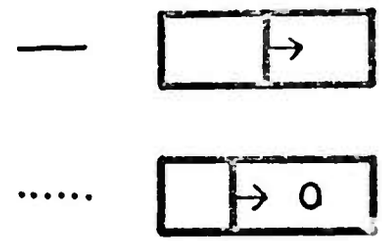

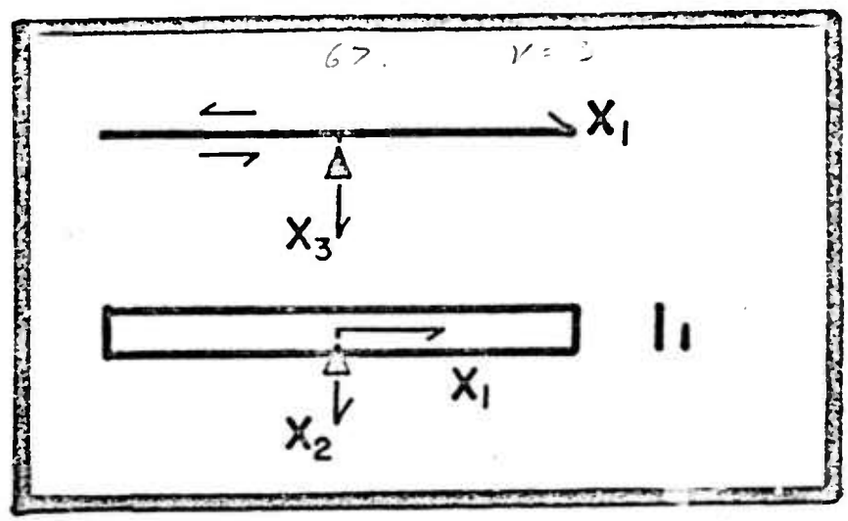

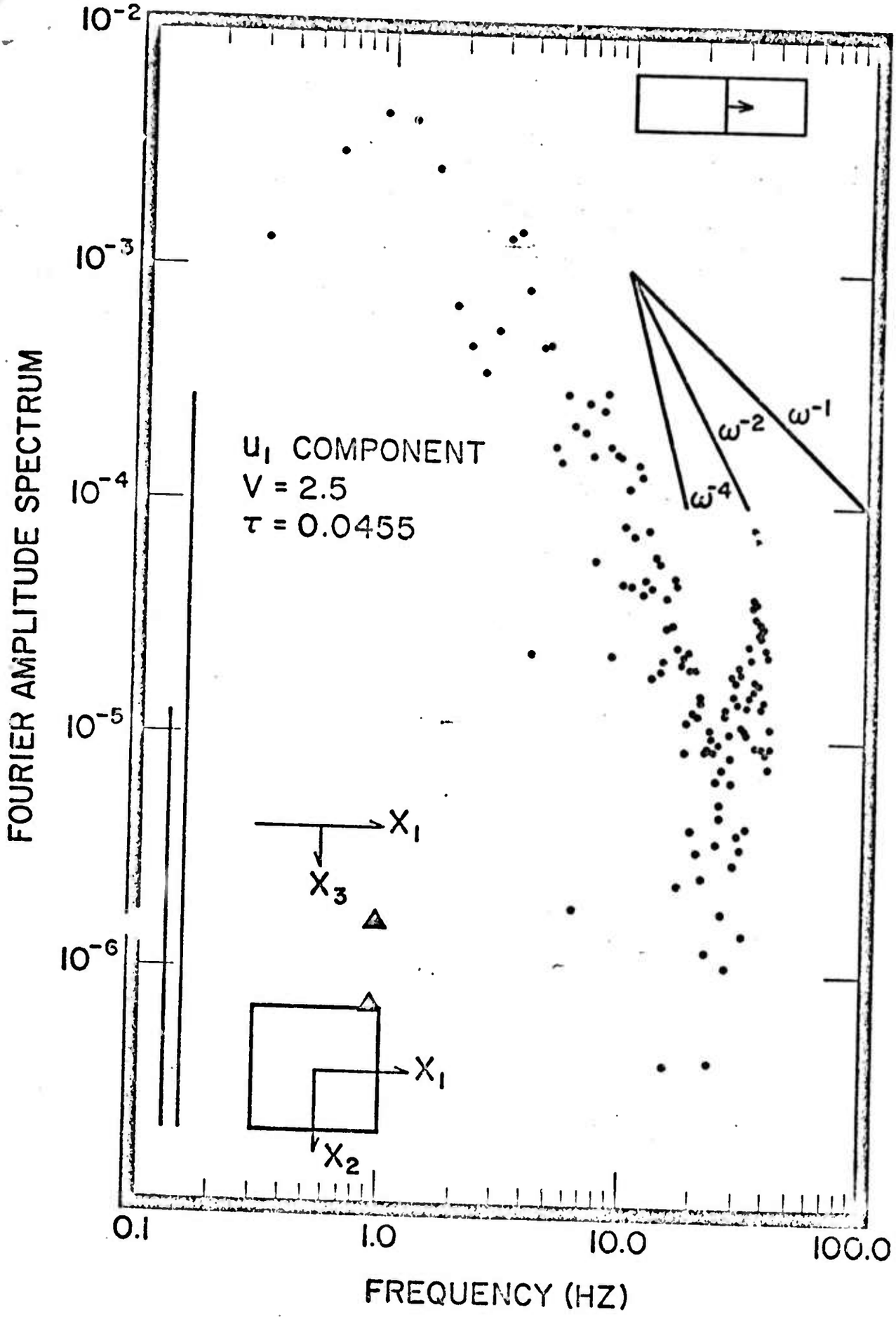
10^{-2}
10^{-3}
10^{-4}
10^{-5}
10^{-6}
FOURIER AMPLITUDE SPECTRUM
u_1 COMPONENT
V = 2.5
τ = 0.0455
ω^{-1}
ω^{-2}
ω^{-4}
X_1
X_3
X_1
X_2
0.1
1.0
10.0
100.0
FREQUENCY (HZ)